Debonding behavior of non-welded wrapped composite X-joints subjected to monotonic tensile load – Numerical study and validation

He, Pei; Wolters, Mees; Waltener, Clement; Pavlovic, Marko

DOI
10.1016/j.engstruct.2024.118969

Publication date
2024

Document Version
Final published version

Published in
Engineering Structures

Citation (APA)
He, P., Wolters, M., Waltener, C., & Pavlovic, M. (2024). Debonding behavior of non-welded wrapped composite X-joints subjected to monotonic tensile load – Numerical study and validation. *Engineering Structures*, *321*, Article 118969. https://doi.org/10.1016/j.engstruct.2024.118969

Engineering Structures 321 (2024) 118969

Contents lists available at ScienceDirect

Engineering Structures

journal homepage: www.elsevier.com/locate/engstruct

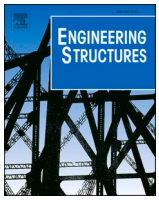

Debonding behavior of non-welded wrapped composite X-joints subjected to monotonic tensile load – Numerical study and validation

Pei He [a], Mees Wolters [b], Clement Waltener [b], Marko Pavlovic [a,*]

[a] Faculty of Civil Engineering and Geosciences, Delft University of Technology, the Netherlands
[b] Tree Composites B.V, the Netherlands

ARTICLE INFO

Keywords:
Wrapped composite X-joints
Circular hollow sections (CHS)
Debonding
Digital image correlation (DIC)
FE models
CZM (cohesive zone modeling)
Four-linear traction-separation law
Numerical validation

ABSTRACT

The dominant failure mode in the non-welded wrapped composite joints made with GFRP composite material wrapped around steel circular hollow sections (CHS) is characterized as interface debonding. However, in the ultimate load joint experiments, debonding process was merely inferred from the surface strain distribution obtained by the digital image correlation (DIC). A thorough understanding and explicit illustration of debonding mechanism in wrapped composite X-joints is needed with help of finite element modeling (FEM), in order to provide prediction models for design of wrapped composite joints in engineering structures. In this paper, two FE models were developed to simulate the debonding behavior of small-scale and medium-scale wrapped composite 45° X-joints in monotonic tensile tests previously conducted by the authors. A new strategy of modeling complex composite geometry using 4-node tetrahedral elements (C3D4) without defining composite lay-up was proposed. The cohesive zone modeling (CZM) approach was utilized to simulate the debonding behavior of composite-steel interface with introduction of a new four-linear traction-separation law. The generated FE models were validated by good agreement between numerical and experimental results in terms of load-displacement response and surface strain distribution throughout the failure process at two joint scales. The validated models gained good insight into the joint debonding mechanism and determined the surface strain threshold for quantifying the debonding length. Development and validation of the FE models with unique set of parameters aligned well with the experiment results at two different scales is an important step for prediction and design of wrapped composite joints.

1. Introduction

The welded circular hollow section (CHS) joints have been extensively used in the jacket structures supporting offshore wind turbines, which are subjected to long-term cyclic loading. There are generally two reinforcing schemes related to welded CHS joints aiming to enhance their load capacity and mitigate stress concentrations and unfavorable failure modes: 1) steel reinforcing scheme, e.g., joints reinforced by steel collar plates [1–4], steel doubler plates [5], etc., and 2) FRP strengthening scheme, e.g., FRP-strengthened CHS T/Y-joints [6–14], X-joints [15–19], Gap K-joints [20,21], and KT-joints [22,23].

Nomenclature

CHS	circular hollow section
FSDT	first-order shear deformation theory
σ	tensile stress in the composite wrap
τ	shear stress at the composite-steel bonded interface
t	thickness of the composite wrap
x	the coordinate in the longitudinal direction along the bonded interface
C3D4	the 4-node linear tetrahedral element
C3D8	the 8-node linear hexahedral element
CZM	cohesive zone modeling
CTOD	crack tip opening displacement
SERR	strain energy release rate
COF	coefficient of friction
"p"	onset of plasticity of the fracture process of the composite-steel bonded interface
"c"	onset of cracking of the fracture process of the composite-steel bonded interface
"b"	onset of fiber bridging of the fracture process of the composite-steel bonded interface

(continued on next column)

(continued)

(continued on next page)

* Corresponding author.
E-mail address: M.Pavlovic@tudelft.nl (M. Pavlovic).

https://doi.org/10.1016/j.engstruct.2024.118969
Received 8 May 2024; Received in revised form 31 July 2024; Accepted 8 September 2024
Available online 16 September 2024

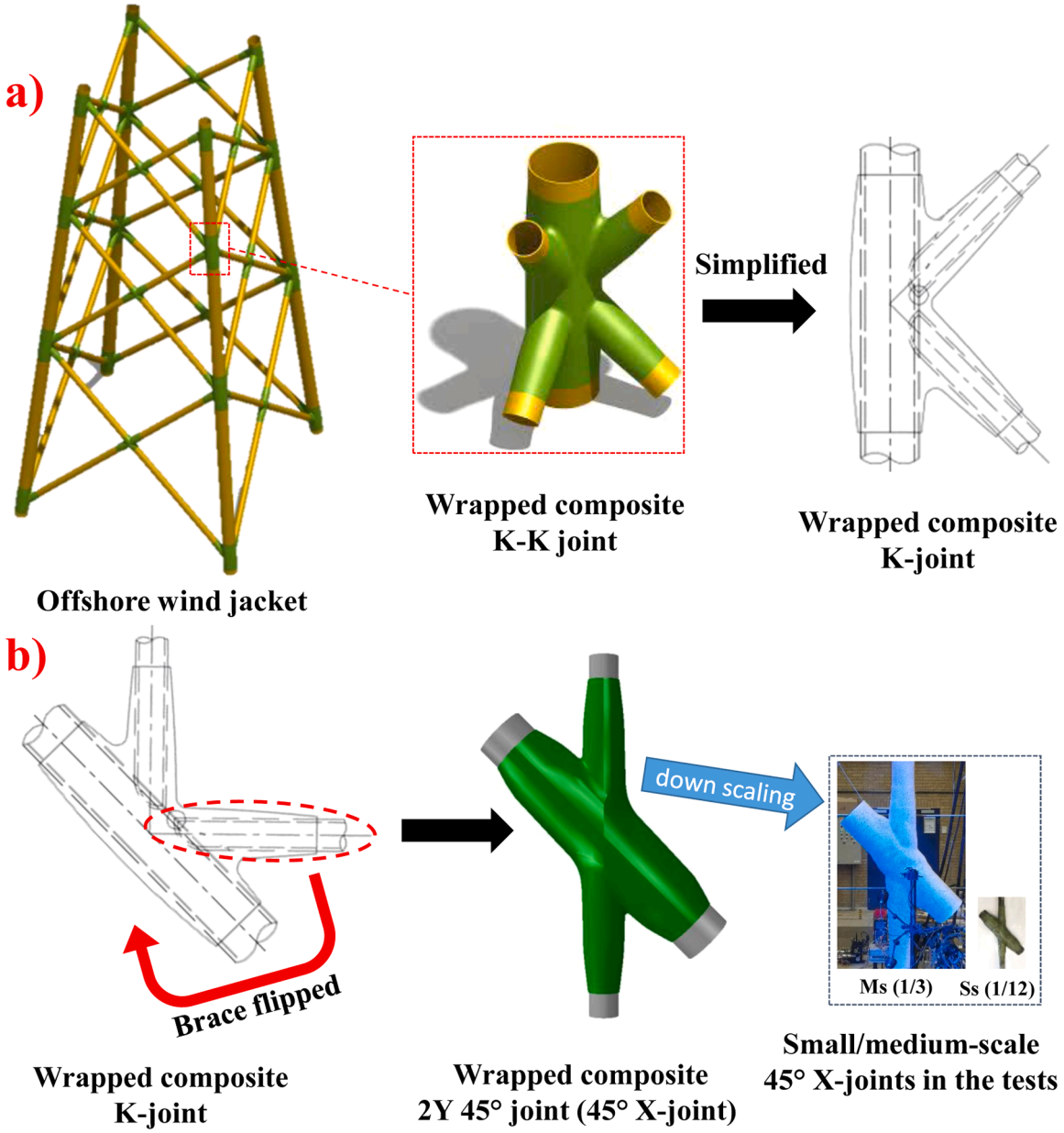

Fig. 1. a) The offshore wind jacket, the full-scale wrapped composite K-K joint [25], and the full-scale wrapped composite K-joint; b) the full-scale wrapped composite 2Y 45° joint (further names as 45° X-joint), and the specimens of wrapped composite 45° X-joints in small-scale (Ss) and medium-scale (Ms) in the ultimate load experiments [26].

(*continued*)

"f"	failure of the fracture process of the composite-steel bonded interface
δ_p, δ_c, δ_b, δ_f	CTOD at the stage of "p", "c", "b", "f"
σ_p, σ_c, σ_b, σ_f	cohesive traction at the stage of "p", "c", "b", "f"
$G_{Ic,tip}$	critical SERR at crack initiation in mode I fracture
G_{Ic}	critical SERR at crack propagation in mode I fracture
$G_{IIc,tip}$	critical SERR at crack initiation in mode II fracture
G_{IIc}	critical SERR at crack propagation in mode I fracture
CSDMG	damage variable of the cohesive interface in ABAQUS
DOF	degrees of freedom
A	linear elastic stage
$\mathbf{l_e}$	elastic load limit
$\mathbf{i_r}$	initiation of debonding from wrap root
B	progression of debonding from wrap root
y	initiation of steel yielding
$\mathbf{i_e}$	initiation of debonding from wrap end
C	peak load

(*continued on next column*)

(*continued*)

r	rupture
cX45	wrapped composite joints, X geometry at 45° angle between braces and chord
S_s, M_s	small-scale, medium-scale joints
F_r	the ultimate load applied on the joint brace
d	brace diameter of the joint
l_{wb}, t_{wn}	Wrapping length on the brace, nominal wrapping thickness

In addition to the above-mentioned strengthening techniques for welded CHS joints, a new type of CHS joint, i.e., wrapped composite joints, has been proposed by the authors [24]. In this innovative joint, the weld is excluded to eliminate the source of notch effects and residual stresses and to fully unlock the application potential of CHS restricted by current welding technology. Unlike FRP-strengthened welded CHS joints, in wrapped composite joints, the steel tubes are connected by a much thicker FRP composite wrapping to ensure that the load is only

transferred through the bonding between the FRP and steel tubes. The wrapped composite joints are designed to be applied in offshore wind jackets, aiming to enhance their fatigue resistance and contribute to the energy transition.

The focuses of studies in terms of wrapped composite joints by the authors [26–28] were on the K-K joint in offshore wind jackets as illustrated in Fig. 1a, which are prone to tensile fatigue failure. Its geometry was simplified to K-joint to limit load conditions to uniplanar tension aiming to facilitate understanding of its failure mechanism. The K-joint was further designed as the 2Y 45° joint as shown in Fig. 1b with comparable stress concentration to allow for application of laboratory uniaxial tensile loads. The 2Y 45° joint was subsequently named as 45° X-joint for simplification of nomenclature. Considering limitations of laboratory machines in terms of load capacity and clamping devices, in the performed lab tests the geometry of the full-scale wrapped composite 45° X-joint was downscaled to 1/3 and 1/12 as the small-scale and medium-scale geometry, respectively [26–28]. The conducted fatigue tests proved superior fatigue endurance of wrapped composite X-joints over welded counterparts [27]. The ultimate load experiments shown improved initial stiffness and elastic load limit of wrapped joints compared to welded connections, and identified debonding of the composite-steel bonded interface as the predominant failure mode [26].

Nevertheless, a comprehensive and thorough understanding of the debonding process in the joints is missing attributed to the limitations of digital image technique (DIC) technique, through which the debonding process can only be inferred implicitly by analyzing the surface strain variation. Finite element modeling should be developed to clarify the debonding process after the FE model is calibrated by the experimental data.

There are two key challenges to conquer in simulating debonding of wrapped composite X-joints: 1) how to model the thick composite wrapping with complex and curved geometry; 2) how to model the bonding behavior of composite-steel bonded interface. The most relevant research studies can be found in the literature regarding simulating FRP-strengthened CHS T/Y-joints [6–14], X-joints [15–19], Gap K-joints [20,21], and KT-joints [22,23]. In these studies the composite wrapping was modeled using either the 4-node conventional shell element (S4R in ABAQUS [29]) [6–12], [20–23] or the 8-node conventional element (SHELL281 in ANSYS [30]) [13–19]. Both element types are shell elements that only enforce the Mindlin-Reissner plate theory also known as first-order shear deformation theory (FSDT) [31–33]. The through-thickness shear deformation is considered to be constant in this case to represent shear modulus characteristics of FRP composites [34]. Using conventional shell elements to model FRP wrapping is applicable in the case of FRP retrofitted joints considering that:

1) the layup configuration can be easily defined since the wrapping thickness is relatively small without significant variation especially at the intersection region (no more than 10 mm);
2) the through-thickness shear deformation of laminates is relatively small since the main load is still transferred by the welds. Therefore, the assumption that the through-thickness shear deformation is constant during the loading process by FSDT would not penalize the modeling results significantly [35].

However, establishing the layup configuration for the composite wrap in wrapped composite joints using conventional shell elements like S4R or SHELL281 is challenging, primarily due to the large variability in thickness and complex geometry, especially in the region where the steel components intersect. The difficulty in building up layup configuration can be overcome by using continuum shell (CS) elements, which possess more nodes to depict the thickness and can be stacked to represent the sublaminates [34]. Nevertheless, as a type of shell elements being incompressible and inextensible, CS elements are not able to deform in thickness direction and therefore simulation of through-thickness shear deformation is penalized. If good accuracy in simulating significant through-thickness shear deformation is required, as in the case of modeling wrapped composite joints, neither conventional nor continuum shell elements suffice [35]. Having a similar topology to CS elements, 3D solid elements are able to accurately capture through-thickness shear behavior, as they do not incorporate the FSDT considering that their thickness is not necessarily constant during analysis. However, an alternative damage criterion should be proposed using 3D solid elements to simulate through-thickness shear behavior. This is because the Hashin damage criteria [36], normally used to simulate damage of composite laminates modeled by thick shell elements in the previous studies [6–8], [12,20], is not able to simulate out-of-plane behavior and is not implemented for solid element in ABAQUS.

Most of the above-mentioned studies [6–14], [22,23] considered the composite-steel interface as a perfect bond state in the finite element modeling (FEM). This strategy is feasible in modeling FRP-strengthened steel joints, as the bonded interface remains intact during the loading process considering that the main load is transferred through welds. Part of these studies [20,21] utilized the surface-based cohesive contact to simulate the interface behavior between composite laminates and steel, but the bond-slip behavior was assumed elastic. Obviously, these two modeling strategies are not applicable to modeling wrapped composite joints, where accurately simulating the progressive debonding of the composite-steel interface is essential. As the debonding of the bi-material interface exhibits non-linear fracture behavior, it cannot be adequately modeled using linear elastic fracture mechanics (LEFM). Instead, the cohesive zone modeling (CZM) approach can be employed to simulate the non-linear interface behavior, where the constitutive behavior of the fracture process zone (FPZ) is defined by a traction-separation law. However, currently the CZM was mainly applied to simulation of delamination within composite laminates [37–42]. Limited studies were conducted on application of CZM to modeling interface behavior between steel and composites [43,44]. The difficulties in using CZM to model debonding between composites and steel surfaces can be summarized in three aspects:

1) High dependency of the traction-separation law on the surface treatment of steel, fiber layup, and types of adhesives;
2) The inherent presence of mode mixity due to loading asymmetry and material asymmetry across the interface [45];
3) Influence of friction on the fracture behavior of the interface.

The research presented in this paper focused on the development of the finite element (FE) model to simulate debonding process of small-scale and medium-scale wrapped composite X-joints subjected to a monotonic tensile load. To accurately simulate the large through-thickness shear deformation of composite wrap, the 4-node tetrahedral (C3D4) element was used. The “smeared crack approach” normally used in modeling concrete was utilized in modeling the composite wrap with complex geometry, where the mesoscale damage of composite plies is equivalently simulated by plastic deformation of the macroscale laminates. The surface-based CZM approach was utilized to simulate the debonding behavior of composite-steel interface with introduction of a new four-linear traction-separation law. The mode I and mode II cohesive laws were obtained through double cantilever beam (DCB) and end notched flexure (ENF) tests, respectively, conducted at the material level by the authors [46,47]. Additionally, mode mixity was taken into account. The FE joint model was validated by good agreement between the experimental and numerical results in both global response and local surface strain distribution throughout the debonding process. The validated joint model revealed the debonding mechanism of wrapped composite joints and determined the threshold of surface strain in quantifying the debonding length in monotonic experiments.

Table 1
Overview of test series of wrapped composite 45° X-joints.

Test series	Specimens	Scale	Figure number of geometries
1	cX45-Ss-T_S1/2/3/4/5	Small-scale	Fig. 2a
2	cX45-Ms-T_S1/2/3	Medium-scale	Fig. 2c

2. Geometry and material of wrapped composite 45° X-joints

This section gives a short review on the configuration of wrapped composite 45° X-joints in monotonic tensile tests performed by the authors in the previous study [26]. Two series of tests are conducted on the small-scale and medium-scale X-joints, respectively, as summarized in Table 1. Geometries of the joints with dimensions are illustrated in Fig. 2. 45° X-joints at small-scale are composed of two CHS 60.3/4 brace members and one CHS 108/5 chord member, while joints at medium-scale consist of two CHS 219/6 brace members and one CHS 324/10 chord member. The joint dimensions at medium-scale are 30 % of the real-scale in off-shore jacket supporting structures for wind turbines, where the brace and chord members are typically within 600–1200 mm range in diameter. At two scales, different values of wrapping length (4 times the brace diameter at small scale, 2.5 times the chord diameter at medium scale) and different values of the parameter 2 L/D (5.6 at small scale, 4.3 at medium scale) were chosen. The aim is to calibrate and validate the unique set of material properties used in the numerical model. The aim of conducting monotonic tensile tests at two scales is to investigate the size effect on the debonding mechanism. The following naming convention of the joint specimens is used: cX45 – wrapped composite joints, X geometry at 45° angle between braces and chord; Ss, Ms – small-scale and medium-scale, respectively; T – monotonic tensile load scenario; S1/2/3/etc. - nominally identical specimens, number 1, 2, 3, etc.

The CHS profiles of all specimens are made of mild steel with grade S355. CHS tubes are connected by E-Glass fiber mixed with thermoset resin with volumetric fraction ranging 30–32 % and wrapped (laminated) around steel hollow sections. It should be noted that the composite wrap is directly bonded on the steel tubes without application of intermediate adhesive layer so that the failure mode related to adhesive is eliminated. Steel tubes are grit blasted and chemically degreased as surface preparation prior to wrapping to ensure good bonding strength between the composite wrap and the steel tubes. The alignment of the steel tubes is controlled to be less than 0.5 mm misalignment. The hand lamination (wrapping) procedure is fulfilled in a couple of steps with quality control to ensure smooth thickness transition, good compaction and avoiding air gaps. The maximum thickness of the composite wrap is 14 mm and 26 mm at small and medium-scale, respectively, at the root location, and decreases to 0 mm at the end of the bonded connection, see Fig. 2. No post-curing is applied to the wrapped specimens. The repeatability of the production is assured by using only certified laminators in the factory where the joints are produced. Temperature, humidity, surface roughness and cleaning, peroxide type and content, resin shell, and cleaning of the glass fiber and mats are strictly controlled through the quality control and assurance program.

E-Glass fiber is composed of bidirectional woven fabric and chopped strand mat to perform quasi-isotropic behavior. The used resin is toughened vinyl ester resin aiming for improvement of the elastic load limit and failure displacement of the joints [48]. Mechanical properties of the mild steel and the composite laminate are summarized in Table 2. The standard tensile/compressive/in-plane shear/double beam shear coupon tests are conducted to obtain these material properties based on ISO standard [49–54].

3. Review of the experimental work

The monotonic tensile tests of wrapped composite 45° X-joints performed by the authors in the previous study [26] are briefly reviewed in this section. An extensive experiment program was conducted to investigate the debonding behavior of the joints at small-scale and medium-scale. Fig. 3 illustrates the test set-up and the failure modes of small-scale X-joints under monotonic tensile load. The specimens are installed in the Universal Testing Machine (UTM) with 800 kN loading capacity equipped with hydraulic clamping heads in Stevin lab 2 of TU Delft. The axial load on braces is applied through gripping the ends by pairs of preloaded steel clamps with pins inside, as shown in Fig. 3b, in order to obtain uniform stress distribution in cross section at load introduction. Load is applied by displacement control with rate of 1 mm/min to provide quasi-static loading condition. The predominant failure mode is full debonding of the bonded interface on the braces (See Fig. 3b), followed by the final pull-out of the steel brace member from the composite wrap.

Fig. 4 shows the test set-up and the failure modes of wrapped composite X-joints at medium-scale. The monotonic tensile experiment is conducted in the 6-meter-high loading frame with 2.5 MN loading capacity. The specimen is pin connected to the loading frame through the ear plates with Ø100 mm cylindrical hole, which are welded through end plates to the braces. Load is applied by controlling the hydraulic jack moving upward, with the displacement control with rate of 1 mm/min to obtain quasi-static loading condition. Similar to small-scale joints, full debonding on the bonded interface on the brace followed by final pull-out of steel brace member from the composite wrap is the predominant failure mode at the medium-scale. In addition, delamination at the root of wrap and at the end of wrap on braces is observed, see Fig. 4b.

In the tests at both scales, the 3-dimensional (3D) Digital Image Correlation (DIC) system is used to measure both longitudinal extension between ends of the specimens and distribution of surface strain of the joints to indirectly track the propagation of the debonding crack, see Fig. 4. GOM Aramis adjustable base 12MPx system is used which includes two cameras with 12-megapixel resolution, controller, and graphical analysis software to acquire and process test data. Two measuring volumes are used corresponding to two scales. The $1900 \times 1400 \times 1400\ mm^3$ measuring volume is utilized in the medium-scale tests, while the $750 \times 610 \times 610\ mm^3$ measuring volume is used in the small-scale tests. Speckle patterns are applied on the specimens' surface by spray method with grain size of approximately 2 and 4 mm in small-scale and medium-scale experiments, respectively, see Fig. 3 and Fig. 4. Polarized blue light is used to limit the influence of variation of ambient light on measurement accuracy. The experimental response and failure mechanism were explained in great detail by the authors [26].

4. Finite element modeling (FEM)

This study employed ABAQUS [29] to simulate debonding behavior of wrapped composite 45° X-joints sustained to monotonic tensile load, due to its excellent performance in non-linear analysis and contact analysis in the present numerical investigations. The through-thickness shear deformation of composite wrap was properly modeled without tedious work to build up layup configuration in complex and curved laminate geometry. The cohesive contact approach was utilized to simulate progressive debonding process. The associated traction-separation law parameters were chosen in accordance with the interface test results conducted by the authors [46,47]. The effectiveness of the joint model was demonstrated.

4.1. Geometries and dimensions

Geometries of the FE models of the 45°X-joints at small-scale and medium-scale are illustrated in Fig. 2b and Fig. 2d, respectively. In order to save computational costs, only half geometry was built for each type

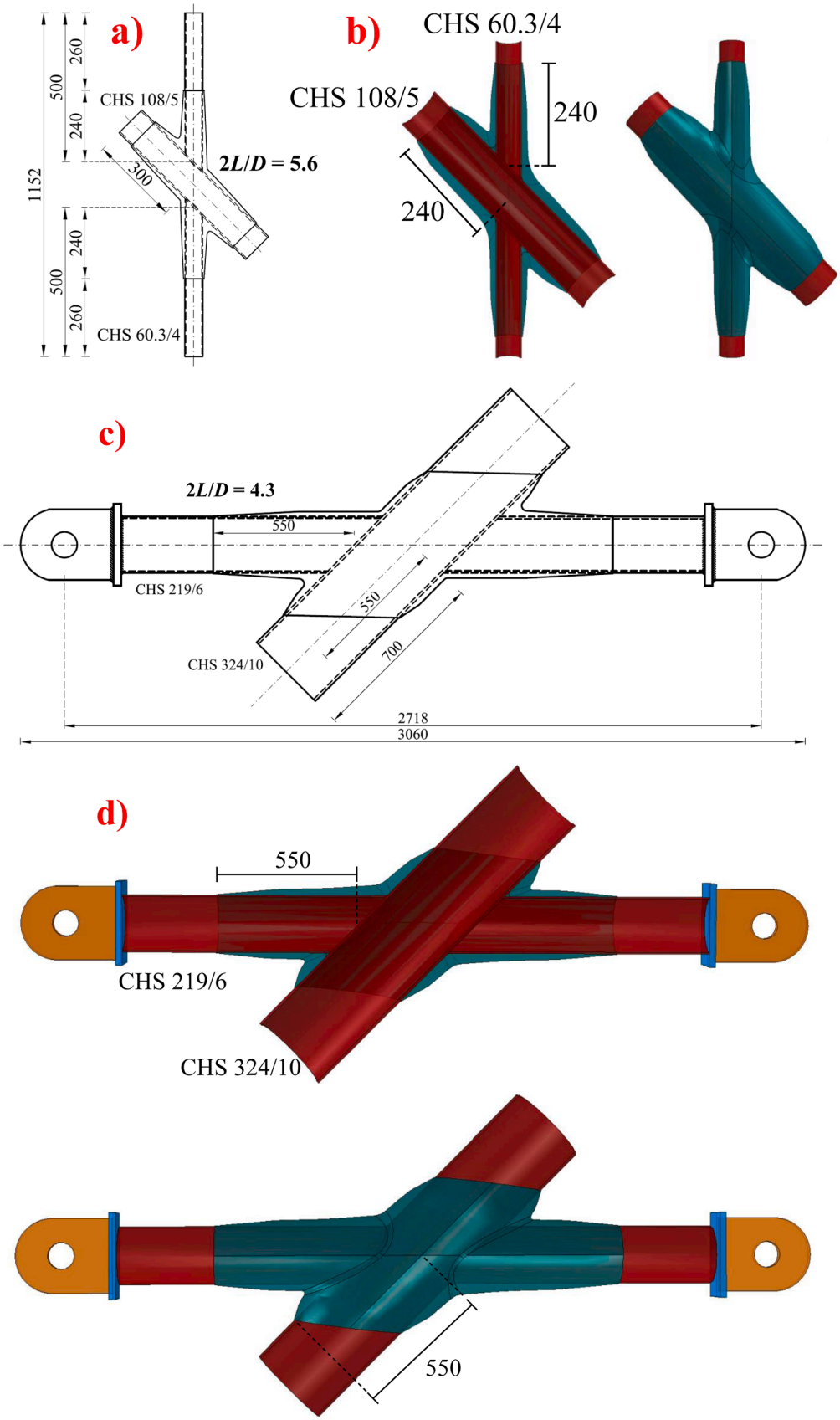

Fig. 2. Geometries of wrapped composite 45° X-joints in monotonic tensile experiments: a) small-scale X-joints in experiments; b) small-scale X-joints in FEM – front and back view; c) medium-scale X-joints in experiments; d) medium-scale X-joints in FEM – front and back view.

Table 2
Mechanical properties of mild steel and composite laminate used in production of wrapped composite X-joints.

Material	Mechanical properties	Average value (and CoV [%])	Standard
Mild steel	Tensile modulus – E	210000 MPa (5.74)	ISO 6892 −1 [49]
	Yield strength – σ_e	360.91 MPa (4.86)	
Composite laminate	In-plane tensile strength in x/y direction – $f_{x,t} = f_{y,t}$	216 MPa (5.78)	ISO 527 −1 [50] and
	In-plane tensile modulus in x/y direction – $E_{x,t} = E_{y,t}$	11798 MPa (6.37)	527 −2[51]
	In-plane compressive strength in x/y direction – $f_{x,c}$=$f_{y,c}$	200 MPa (3.79)	ISO 14126[52]
	In-plane compressive modulus in x/y direction – $E_{x,c}$= $E_{y,c}$	12077 MPa (4.50)	
	In-plane shear strength – $f_{xy,v}$	72.2 MPa (2.59)	ISO 14129[53]
	In-plane shear modulus – G_{xy}	3120 MPa (6.81)	
	Out-of-plane shear strength – $f_{xz,v}$	35.74 MPa (4.85)	ISO 19927[54]
	Out-of-plane shear modulus – G_{xz}	2686 MPa (7.35)	

of joint, based on the original geometry. The dimensions of the circular hollow sections and the composite wrap in the models are consistent with those in the experiments to eliminate the influence of joint geometry on the modeling results.

4.2. Boundary conditions, load application and analyses method

The boundary conditions used in the FE models of small-scale and medium-scale 45° X-joints are illustrated in Fig. 5b and Fig. 6b, respectively, compared to experimental set-up shown in Fig. 5a and Fig. 6a. At both scales, the symmetry boundary condition in the global Z direction is applied to the mid-plane of the joint's half geometry, with respect to the symmetric tensile load.

In the tensile test of small-scale 45° X joints, the load is transferred through gripping the brace members by the steel clamps. Since no sliding occurs between the clamps and the braces, simplified boundary conditions are used where geometry of the clamps, pins, and the part of braces gripped in between are not considered. Two reference points (RPs), named "Top" and "Bottom", are created at the center of the circular cross-sections of the top and bottom braces, which are positioned on the edges of the steel clamps. The circular cross-sections are kinematically constrained (coupled) to the two RPs in all degrees of freedom to replicate the load transfer in the tests. The displacement-controlled failure loading in experiments is replicated by imposing displacement/rotation boundary conditions at the RPs "Top" and "Bottom". The negative vertical displacement (U2) is applied to the RP "Bottom" while the in-plane rotation UR3 is released at both RPs "Top" and "Bottom" to simulate the load application as in the tests. It should be noted that 2/3 is designation for the global Y/Z direction. All other degrees of freedom (DOF) at the two RPs are fixed. The values of the vertical displacement (U2) and the vertical reaction force (RF2) at the RP "Bottom" are extracted for analysis of the joint global response.

In the medium-scale joint model, the stiffness of the steel ear plates (the orange parts), and the steel connection plates (the blue parts) cannot be regarded infinite compared to the joints, see Fig. 6. Therefore, their geometries are included in the joint model to ensure good matches of global stiffness to the test results. Two RPs, "Top" and "Bottom", are created at the center of the hollow cylinder of the top and bottom ear plates, respectively, and are kinematically constrained (coupled) to the hollow cylindrical surfaces in all degrees of freedom to replicate the load transfer in the tests. The displacement-controlled failure loading in experiments is replicated by imposing the displacement/rotation boundary conditions at the RPs "Top" and "Bottom". The positive vertical displacement (U2) is applied to the RP "top" to replicate the load application as in the tests, while the in-plane rotation UR3 is released at both RPs. All other DOF are fixed. To allow for analysis of the joint global behavior, the vertical reaction force (RF2) is extracted at the RP "top", while the vertical displacements (U2) are extracted from points located 100 mm away from the two RPs, "Top" and "Bottom", aligning with DIC measurements in the experiments, as shown in Fig. 6b.

Monotonic failure analysis of the joints is modeled in the quasi-static manner using the ABAQUS/Explicit solver [29] because it does not have the usual convergence issue as does the Implicit solver. To enhance the computational efficiency, the massing scaling method is utilized. However, this method tends to increase the inertia forces in the modelling and sometimes leads to useless results. A compromise should be found between the acceptable computational costs and the quality of the results. In the present study, mass scaling with desired time increment of 0.002 s is finally used in the joint modeling. Quality of the modeling results is verified by matching applied and reaction forces during the displacement application process. The desired time increment is selected when a linear match is reached between input and output forces with no fluctuations, as shown in Fig. 7.

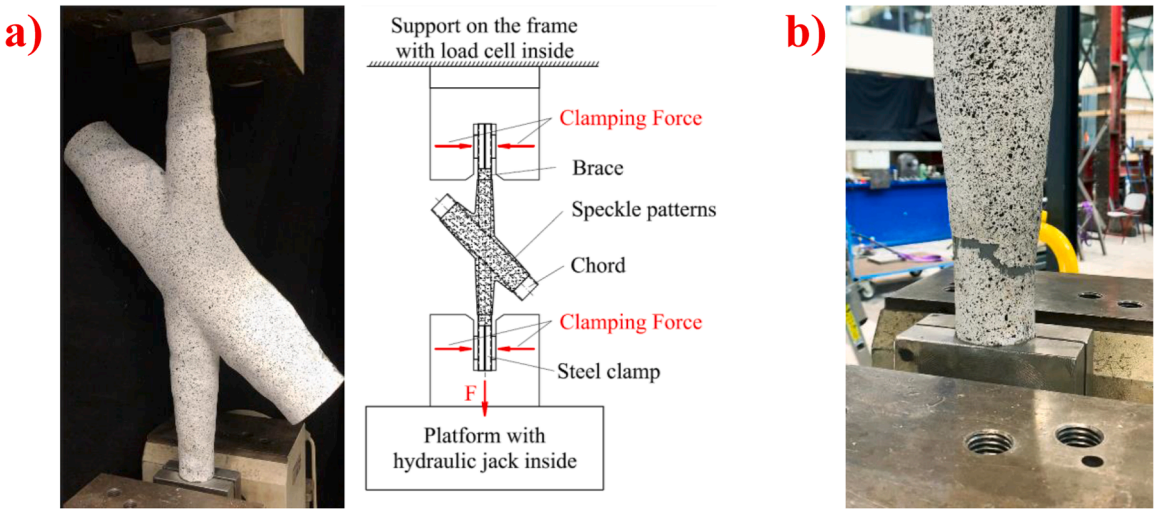

Fig. 3. Monotonic tensile experiments of wrapped composite X-joints at small-scale: a) test set-up; b) failure modes [26].

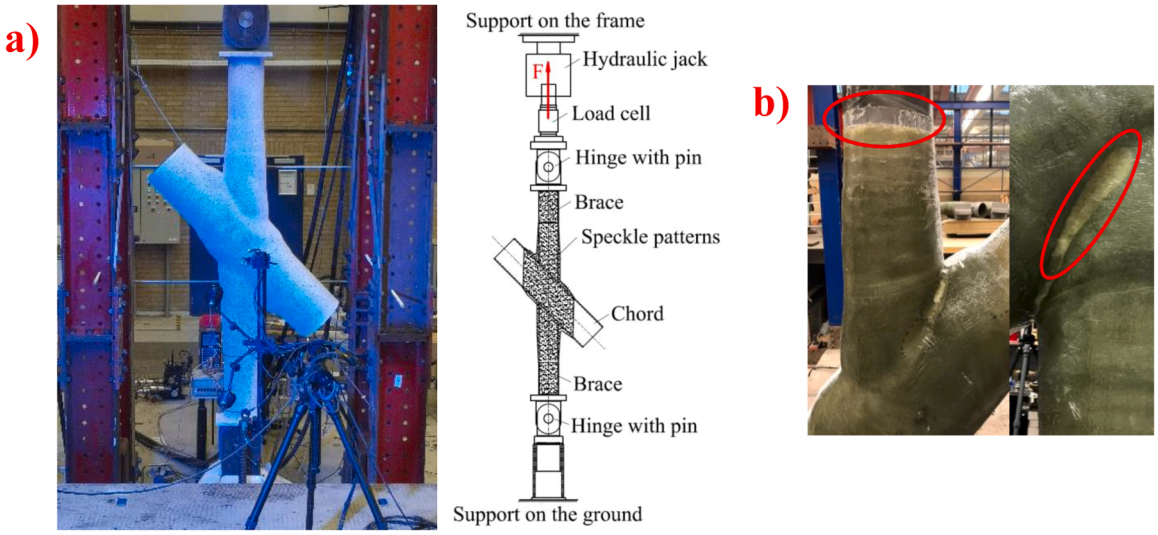

Fig. 4. Monotonic tensile experiments of wrapped composite X-joints at medium-scale: a) test set-up; b) failure modes [26].

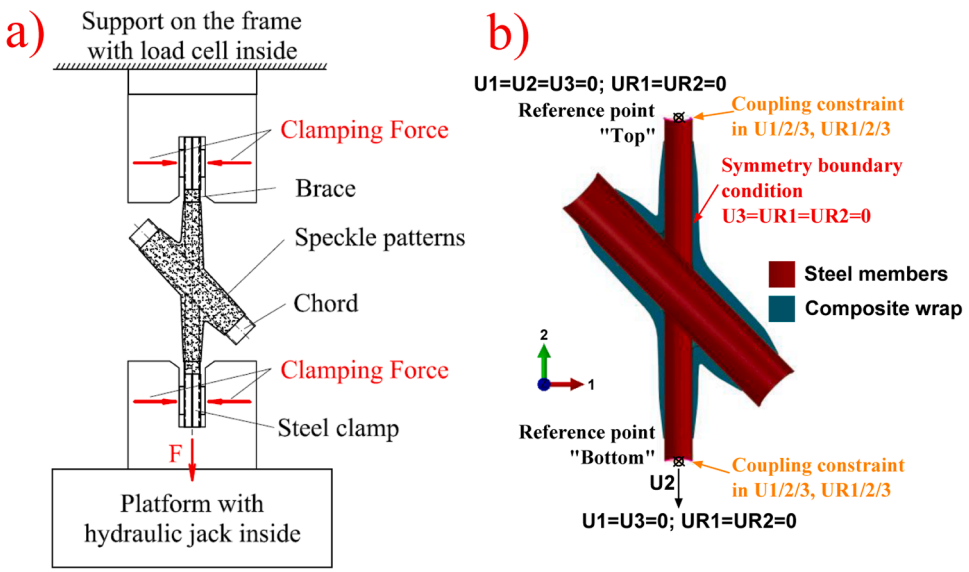

Fig. 5. Boundary conditions in b) the FE model of small-scale 45° X joints based on a) experimental set-up.

4.3. Modeling strategy of composite wrap and steel tubes

A notable characteristic of wrapped composite joints compared to FRP-strengthened joints [6–14], [20–23] is the significant through-thickness shear deformation of composite wrap due to absence of welds. The reason of the considerable through-thickness shear deformation within the composite wrap is explained with reference to Fig. 8a ~ Fig. 8c. Fig. 8a illustrated the equilibrium of an infinitesimal element of composite wrap, and the equilibrium is expressed in Eq. 1: [55].

$$\frac{d\sigma}{dx} = \frac{\tau}{t} \tag{1}$$

where σ and τ are the tensile stress in the composite wrap and the shear stress at the interface, respectively, t is the thickness of the wrap, and x is the coordinate in the longitudinal direction. Fig. 8b and Fig. 8c show the through-thickness shear stress distribution along the thickness of the composite wrap at the crack tip, the bonded region, and the debonded region, generated from the calibrated FE model. In an idealistic case without friction at the cracked interface, the load is transfer merely by the axial stress of the wrap ($d\sigma = 0$), and the shear stress τ at the cracked interface is equal to 0. Consequently, the through-thickness shear stress at the debonded region is rather low and is increased slightly close to the interface due to friction effect, as shown in Fig. 8b. In the bonded region, the shear stress τ at the interface is significant either due to bonding or friction at the bonded interface. Therefore, the through-thickness shear stress within the wrap is more pronounced than the debonded region, see Fig. 8b. The through-thickness shear stress τ at the crack tip is dominated, as shown in Fig. 8b, attributed to the axial stress concentration of the composite wrap and the shear stress concentration at the interface in this location. It should be noted that large through-thickness shear stress τ within the wrap leads to significant decrease of its thickness t. If the composite wrap is modeled using shell element being incompressible and inextensible, simulation of large through-thickness shear deformation of composite wrap is prohibited, meaning that accurate simulation of debonding on the interface is hindered. Conversely, 3D solid elements can be used to capture this behavior accurately, which do not incorporate the FSDT as their thickness is not necessarily constant during analysis and are selected to model composite wrap in the present

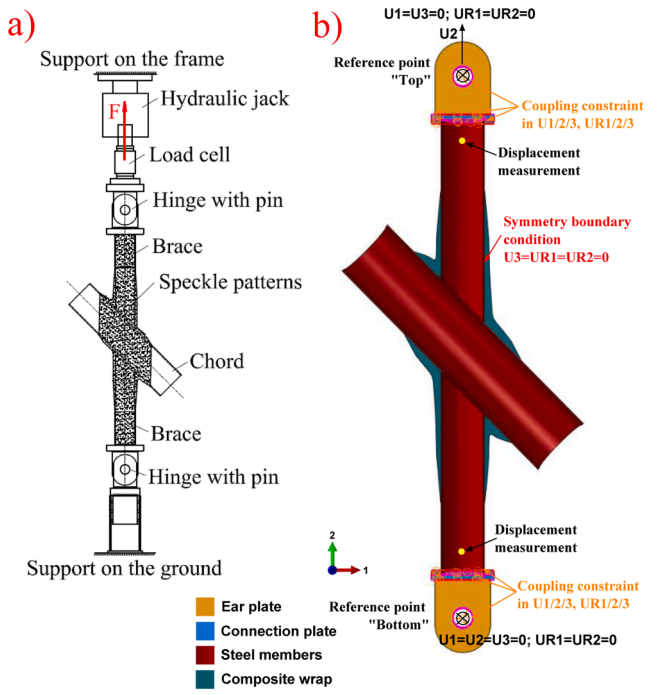

Fig. 6. Boundary conditions in b) the FE model of medium-scale 45° X joints based on a) experimental set-up.

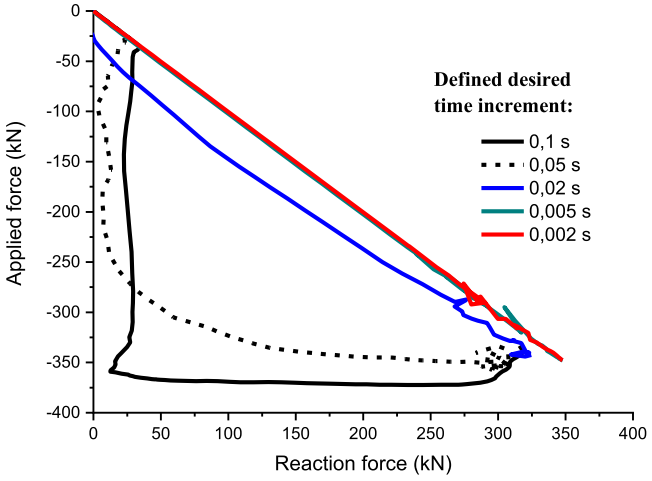

Fig. 7. Quality of quasi-static solution – an example of small-scale joint modeling.

simulation work.

There are two strategies to build the geometry of the composite wrap using solid elements.

1) A mesoscale model: build the geometry of all plies within the composite laminates and each ply is meshed with solid elements individually.
2) A macroscale model: create the geometry of composite wrap as a bulk piece to equivalently model the behavior between plies, without defining layup configuration of the laminates. Meshing is generated in the entire balk piece.

Creating a detailed layup geometry for the composite wrap is rather challenging, especially when dealing with its complex geometry at the region where steel members intersect, as well as in the region where the composite wrap tapers off to zero thickness. Even if individual plies were built, the constitutive law needed to simulate delamination between adjacent plies remains unknown, introducing additional material input to the joint model. Moreover, aspect ratio limitations exist when using a solid element to mesh an individual composite ply. A lamina should not have the other two dimensions larger than about 10 times the thickness. This would lead to a very refined mesh, resulting in a computationally expensive solution [34]. To prevent these problems, the second strategy is utilized in the current joint modeling.

Fig. 9 visualizes the above-mentioned modeling strategy and mesh of composite wrap and steel hollow sections. The 4-node linear tetrahedral (C3D4) element is used in meshing the composite wrap. The tetrahedral element adapts well to the varied thickness of laminate in the complex intersection region where it is challenging to mesh using hexahedral elements. To accurately capture large through-thickness shear deformation of composite laminate as a consequence of stress concentrations at the crack tip, a relatively fine element size (2 mm in the small-scale FE model and 4 mm in the medium-scale FE model) is used to mesh the composite wrap in the region close to the bonded interface. To save computational costs, the element size of composite wrap gradually increases towards the outer surface (8 mm in the small-scale FE model and 16 mm in the medium-scale FE model), see the zoom-in view in Fig. 9. The mesh size used was determined through a trade-off analysis involving considerations of simulation accuracy, computational cost, and the dimensions of the joint geometry in a mesh sensitivity study performed by the authors [56]. The mesh sensitivity analysis also indicated that the variable mesh size is applicable since it helps enhance computational efficiency without sacrificing modeling accuracy. A comparison between the numerical results using linear and quadratic elements showed that, given the utilization of a relatively fine mesh, linear elements do not significantly reduce numerical accuracy. The brace and chord members were meshed by the 8-node hexahedral (C3D8) element with constant size (2 mm in small-scale and 4 mm in medium-scale). A local seed of 4 elements is assigned to the through-thickness direction to accurately simulate its bending deformation, as shown in Fig. 9.

4.4. Modeling strategy of composite-steel interface

The cohesive contact approach was employed to simulate behavior of the composite-steel bonded interface, which is primarily applied to situations as in wrapped composite joints where the interface thickness is negligibly small. In this approach, the traction-separation law introduced by CZM is assigned to the contact surface pairs. The contact surfaces consist of the inner surface of the composite wrap and the outer surface of the CHS members, as depicted in Fig. 10.

In the simulation of the progressive debonding failure process of wrapped composite joints, the additional slip resistance provided by friction at the bonded interface is non-negligible. Residual confinement of wrap arising from contraction of the composite laminate on the steel tubes enhances the frictional resistance of the bonded interface. Contraction of the composite laminate is recognized to stem from the curing process of the composite laminate during manufacturing of the joint as well as from Poisson's ratio effects of the composite wrap generated from the tensile load application. In the current modeling, the additional slip resistance of the bonded interface provided by friction was considered by assigning the coefficient of friction (COF) to the contact surface pairs illustrated in Fig. 10. A sensitivity analysis in terms of the value of COF was performed by the authors in the joint modeling to validate the contribution of friction to the debonding resistance [56]. The COF was increased from 0 (frictionless) to 0.6 with an increment of 0.1. The results showed that the ultimate load of the joints increased monotonically with the increase in COF, and the ultimate loads in the case of COF = 0.6 were 33 %~75 % larger than in the frictionless case. To determine the COF values used in the joint modeling, a COF test was conducted using the Rtec MFT-5000 tribometer in Stevin Lab 2 at TU

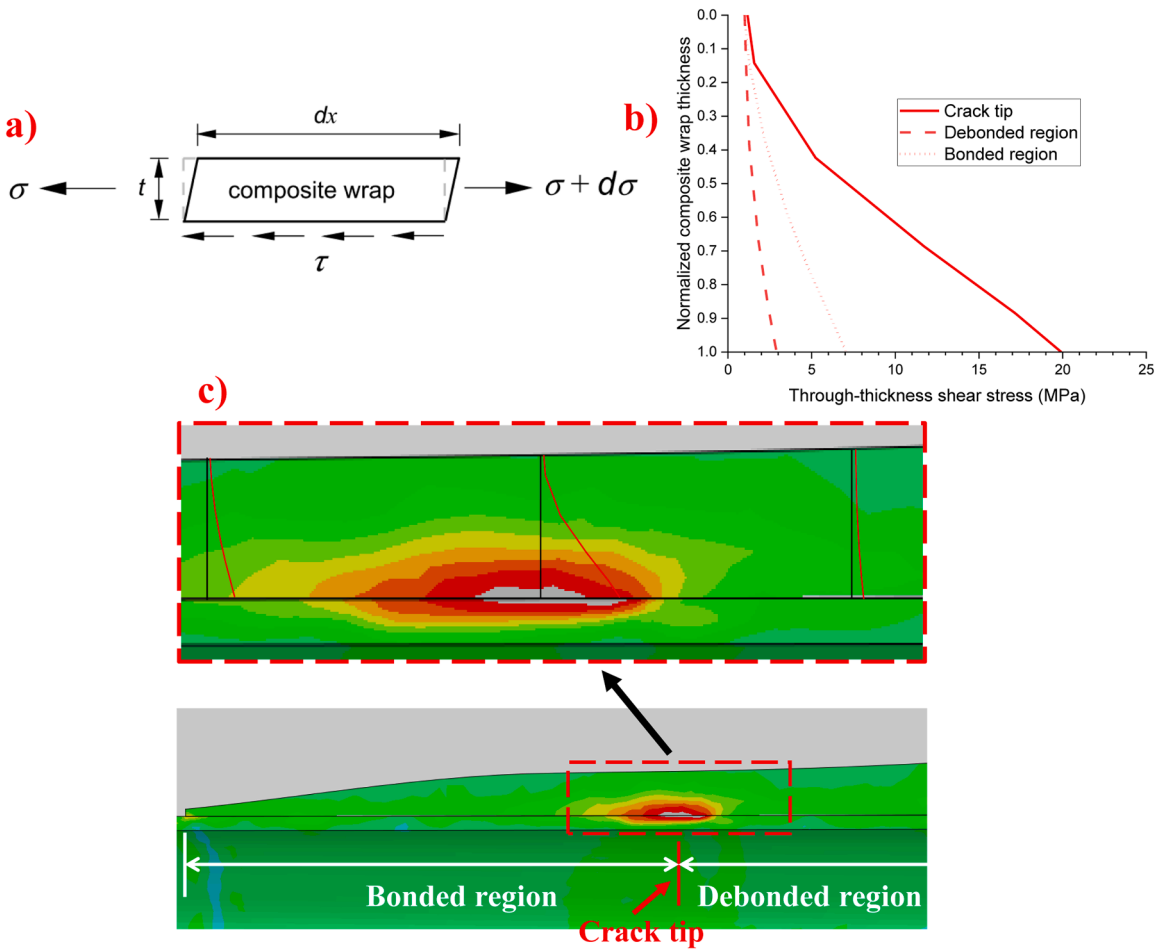

Fig. 8. Explanation of significant through-thickness shear deformation within the composite wrap of wrapped composite joints: a) equilibrium of an infinitesimal element of composite wrap [55]; b) through-thickness shear stress distribution along the normalized thickness of composite wrap at the crack-tip, the debonded region and the bonded region; c) Sketches of the through-thickness shear stress from the FE model.

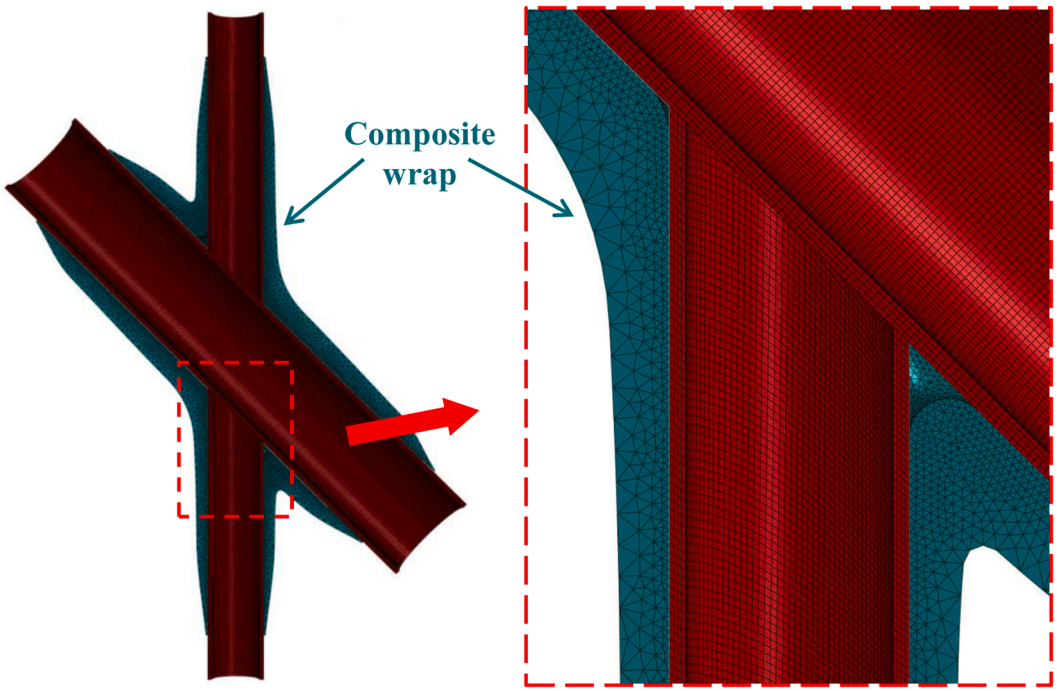

Fig. 9. Modeling strategy and mesh in composite wrap and circular hollow sections – the 45° small-scale X-joint model as an example.

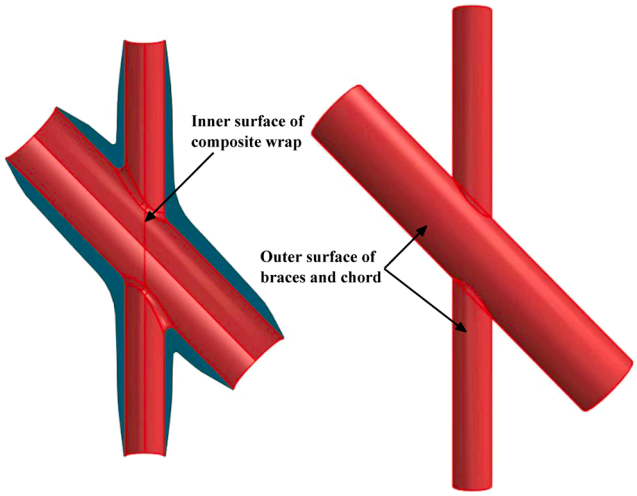

Fig. 10. Contact surface pairs assignment in cohesive contact approach – an example of small-scale 45° X-joint model.

Delft [56]. The test coupons were composed of steel and composite plates, which were cut from the debonded interface of the joints after the monotonic tensile tests, with a contact surface of 25 mm × 10 mm. The test results indicate that the value of COF between composite wrap and steel is within the range of 0.5–0.6.

4.5. Material model of composites, steel, and composite-steel interface

As explained in Section 4.3, using shell elements to simulate considerable through-thickness shear deformation in the composite wrap is inconceivable due to their incompressibility and inextensibility. Alternatively, 3D solid elements can accurately capture this behavior, as they do not employ the FSDT since their thickness varies throughout the analysis. However, an alternative damage criterion should be proposed using 3D solid elements to simulate through-thickness shear behavior. This is because the Hashin damage criteria [36], normally used to simulate damage of composite laminates modeled shell elements [6–8, 12, 20], is not able to simulate out-of-plane behavior and is not implemented for solid element in ABAQUS.

In the present research study, the smeared crack approach [57,58] was utilized in modeling the material behavior of the composite wrap. It assumes the cracked composite material to remain a continuum and relies on the modification of the mechanical properties of the composite laminate at the meso-scale (stiffness degradation) to account for the effect of cracking within composite plies and delamination between adjacent plies at the micro-scale. In other words, the anisotropic plasticity model is used in the current study to equivalently simulate the overall softening behavior of the composite laminate due to the combination of damage occurring at the micro-level of matrix, fibers and the interlaminar interfaces. Using the anisotropic plasticity model with 3D

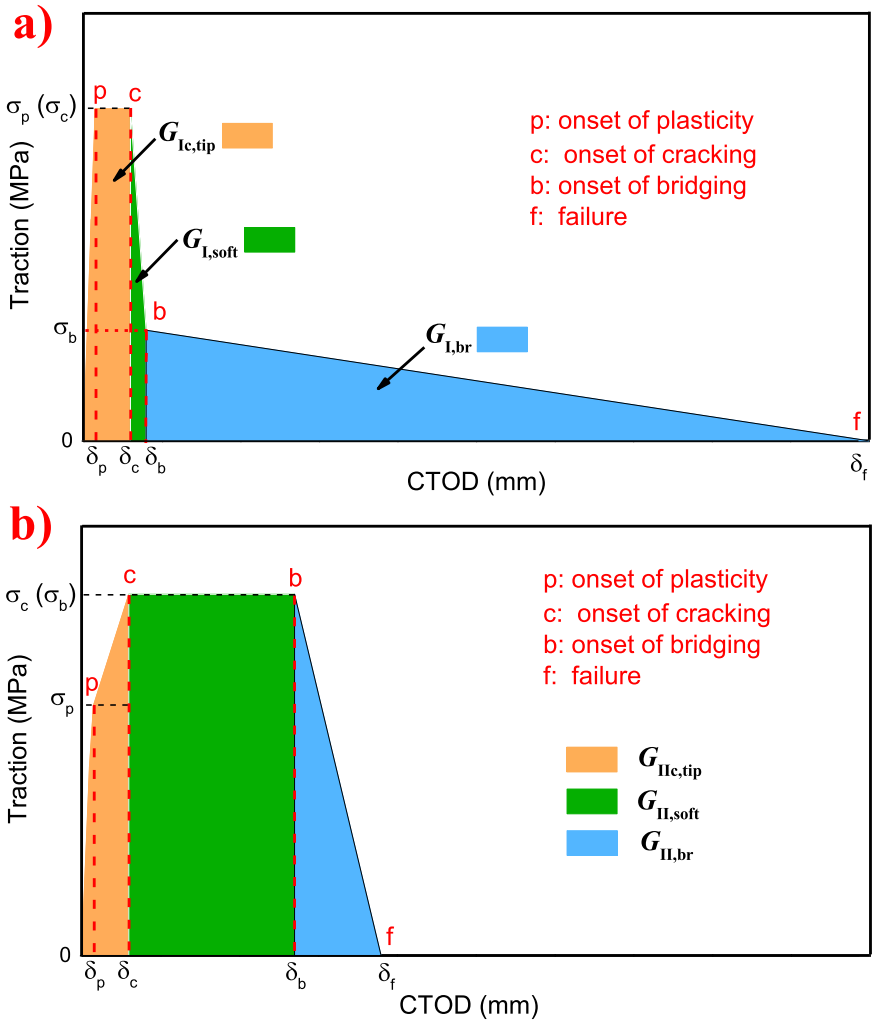

Fig. 11. Schematic view of the cohesive laws in a) pure mode I and in b) pure mode II [46,61].

Table 3
Cohesive parameters of the cohesive laws in mode I and mode II fracture process of composite-steel bonded interface [46,47].

	Onset of plasticity - stage "p"		Onset of cracking - stage "c"		Onset of fiber bridging - stage "b"		Failure - stage "f"		Critical SERR	
Mode I	δ_p (mm)	σ_p (MPa)	δ_c (mm)	σ_c (MPa)	δ_b (mm)	σ_b (MPa)	δ_f (mm)	σ_f (MPa)	$G_{Ic,tip}$ (N/mm)	G_{Ic} (N/mm)
	0.0015	14.67	0.012	14.67	0.054	1.47	0.394	0	0.17	0.76
Mode II	δ_p (mm)	σ_p (MPa)	δ_c (mm)	σ_c (MPa)	δ_b (mm)	σ_b (MPa)	δ_f (mm)	σ_f (MPa)	$G_{IIc,tip}$ (N/mm)	G_{IIc} (N/mm)
	0.0015	14.67	0.025	22	0.069	22	0.087	0	0.45	1.6

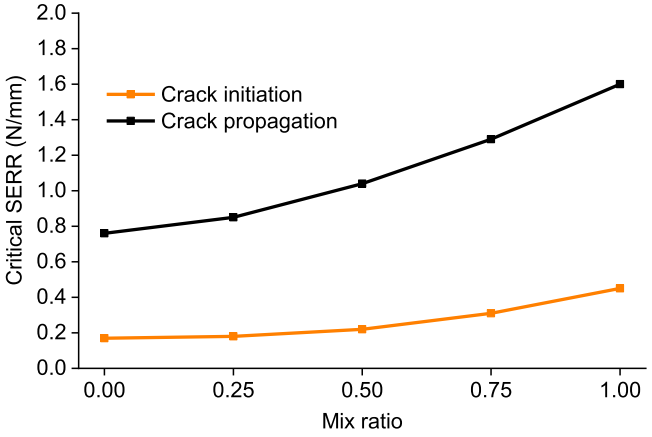

Fig. 12. Strain energy release rate for crack initiation and crack propagation in function of mode mix ratio in CZM.

solid elements to simulate the material behavior of composite wrap in ABAQUS is based on the three prerequisites:

1) The joint model is subjected to monotonic loading, thereby circumventing any differences in permanent deformation within the material due to plasticity or damage resulting from a hysteretic load.
2) The composite laminate used in wrapped composite joints exhibits significant non-linear behavior, particularly in the through-thickness shear direction, owing to enhanced fracture toughness of resin and design of the composite ply material and configuration.
3) The composite wrap is deliberately designed with sufficient thickness to prevent major crack. This ensures the feasibility of employing the smeared crack approach in the current modeling.

The mechanical characteristics of the anisotropic plasticity model for the composite laminate in ABAQUS are determined based on the results of the material coupon tests summarized in Table 2. To validate the anisotropic plasticity model, it is incorporated into a $4 \times 4 \times 2$ mm cuboid part in ABAQUS meshed with C3D4 elements. Good agreement is reached between the numerical stress-strain curves and the coupon experiment stress-strain curves in terms of various loading scenarios (in-plane tensile, in-plane shear, and out-of-plane shear loads [56]).

The non-linear behavior of steel tubes is simulated by an isotropic plasticity model in ABAQUS. The elasticity properties for a S355 steel grade such as the elastic modulus (E = 210 GPa), nominal yield stress (f_y = 355 MPa) and nominal ultimate stress (f_u = 510 MPa) in combination with isotropic hardening are defined in the plasticity model.

A four-linear traction-separation law is introduced to simulate the fracture process of the composite-steel bonded interface with three distinct phenomena: 1) crack tip deformation [40], [59], [60], 2) softening [46], [47], and 3) fiber bridging [59]. They are distinguished by four critical stages: "p" – onset of plasticity; "c" – onset of cracking; "b" – onset of fiber bridging; "f" – failure. The shape of the cohesive laws in pure mode I and mode II are shown in Fig. 11a and Fig. 11b, respectively, with the cohesive parameters summarized in Table 3. They were obtained through double cantilever beam (DCB) and end notched flexure (ENF) tests, respectively, conducted at the material level by the authors [46], [47]. It can be seen that fiber bridging is governing in mode I, while the softening phenomenon contributes the most to the fracture toughness in mode II.

Table 4
Overview of global response in experiments vs FEA of 45° X joints at the small-scale and the medium-scale.

Specimen or FE model	Initial stiffness [kN/mm]	Elastic load limit [kN]	Ultimate load [kN]
cX45-Ss-T_S1	159.0	183.9	339.5
cX45-Ss-T_S2	163.3	182.2	346.5
cX45-Ss-T_S3	160.3	180.5	347.4
cX45-Ss-T_S4	171.9	180.4	346.0
cX45-Ss-T_S5	170.3	184.9	344.9
Average (and COV [%])	164.9 (3.15)	182.4 (0.98)	345.7 (1.01)
cX45-Ss-T_FEM	173.4	182.1	346.5
Deviation (%)	5	0.1	0.2
Specimen or FE model	Initial stiffness [kN/mm]	Elastic load limit [kN]	Ultimate load [kN]
cX45-Ms-T_S1	349.2	1193	1483
cX45-Ms-T_S2	345.2	1139	1353
cX45-Ms-T_S3	341.5	1053	1640
Average (and COV [%])	345.3 (0.92)	1128 (5.11)	1492 (7.88)
cX45-Ms-T_FEM	351.4	1048	1659
Deviation (%)	2	7	11

Determining mode mixity of the fracture behavior of the bonded interface is essential for simulating debonding of wrapped composite joints, given its prevalence in the bi-material fracture problem. In the current modeling in ABAQUS, the mode mixity is defined in the manner of energy [29], with the mix ratio determined as a ratio of the critical strain energy release rate (SERR) in the shear direction to the total critical SERR. Five mix ratios, i.e. 0 (pure mode I), 0.25, 0.5, 0.75 and 1 (pure mode II), are included in the cohesive zone modeling. The relationship between the critical SERR and the mix ratios is defined as exponential to be aligned with the findings in the current literature [37], see Fig. 12.

5. Validation of FE models of small-scale and medium-scale 45° X-joints

The modeling strategy and input parameters presented in Section 4 are validated by comparing the joint numerical results to the joint experimental results. This comparison encompasses the load-displacement response, the debonding crack pattern at the composite-steel interface and the analysis of surface strains.

5.1. Comparison of load-displacement response

Table 4 summarizes the comparisons involving global response aspects in terms of initial stiffness, elastic load limit and ultimate resistance between the FE models and experimental tests at both the small-scale and the medium-scale. A comparison of the load-displacement curves obtained from the FE models versus the curves from joint experiments is shown in Fig. 13. The elastic load limit in the FE model is

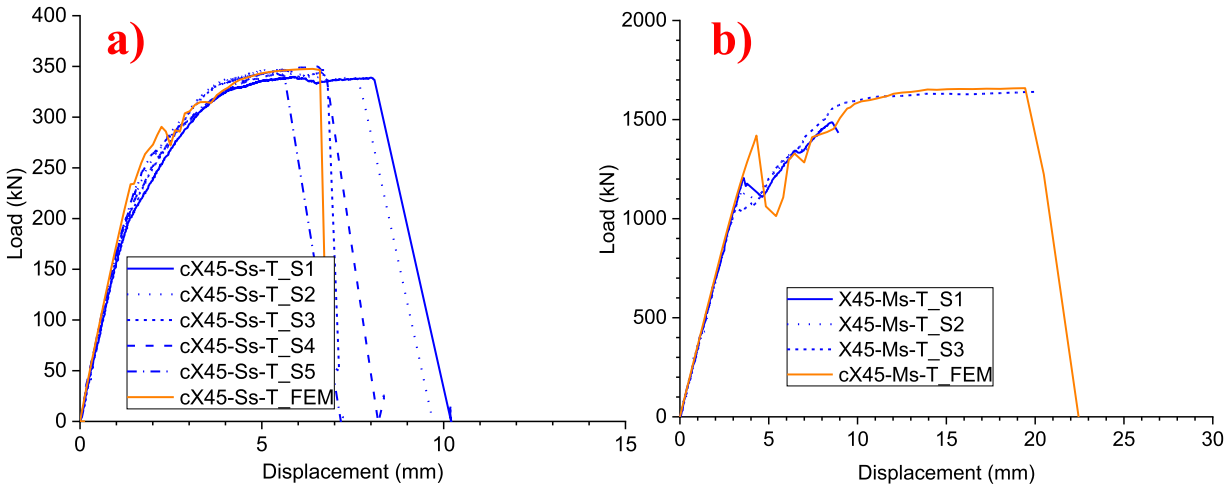

Fig. 13. Load-displacement response of 45° X joint experimental tests and FE models at the a) small-scale and b) medium-scale.

determined by analyzing the stiffness of the load-displacement response combined with the analysis of the damage variable (CSDMG) of the bonded interface. The point on the load-displacement curve where the decreasing rate of tangential stiffness suddenly grows and the crack starts to initiate, as indicated by the CSDMG value, is identified as the elastic load limit.

Table 4 indicates that the initial stiffness and the elastic load limit from numerical simulation match well with the average values in experiments, with a deviation ranging within 5 % and 7 %, respectively. Fig. 13 shows scattering in ultimate resistance and failure displacement in small-scale and medium-scale test specimens. This scattering is due to variations in the coefficient of friction (COF) and mode II interface fracture toughness among the tested specimens. To elaborate on these variations, we have conducted model updating and sensitivity analysis in terms of COF and mode II fracture toughness, see Section 6 for details. In this Section, to facilitate comparison of the debonding process, we fit the small-scale and medium-scale FE models to individual test specimens (X45-Ss-T_S4 at small-scale and X45-Ms-T_S3).

It can be seen from the comparison of debonding process below that at both scales, the joint fails due to full debonding on the braces. The difference in the failure process is that debonding on the chord is mild featuring more moderate softening after the elastic stage (200–300 kN) at small-scale, while it is more sudden at medium-scale with a load drop occurring between 3–7 mm applied displacement, as shown in Fig. 13. The reasons are twofold: a) different values of 2 L/D of the chord members at two-scale which influence the interaction of chord ovalization and chord debonding; b) different ratios of chord diameter to wrapping thickness. At the medium scale, the relative wrapping thickness is smaller, making debonding on the chord more pronounced.

In summary, the global response of the joints obtained by the FE model exhibits an acceptable relationship with the experimental test results, thereby validating the selected modeling strategy and the associated input parameters. This conclusion provides impetus for a more in-depth comparison of the models and experiments in the following section, delving into the composite-steel interface debonding process.

Table 5
Displacement and load magnitude at the critical stages of the debonding process in FE models and experimental tests.

Critical stages		Small-scale		Medium-scale	
		X45-Ss-T_S4	X45-Ss-T_FEM (and deviation [%])	X45-Ms-T_S3	X45-Ms-T_FEM (and deviation [%])
Elastic load limit (stage $\mathbf{l_e}$)	Disp. (mm)	1.11	1.05 [5.4]	3.31	2.98 [10.0]
	Load (kN)	180.4	182.09 [0.9]	1053	1048 [0.5]
Initiation of debonding from wrap root (stage $\mathbf{i_r}$)	Disp. (mm)	1.78	1.49 [16.3]	4.64	5.82[25]
	Load (kN)	234.4	234.2 [0.3]	1106	1108 [0.2]
Initiation of steel yielding (stage **y**)	Disp. (mm)	3.84	3.76 [2.1]	9.09	9.83[8]
	Load (kN)	321.5	321.6 [0.03]	1571	1579 [0.5]
Initiation of debonding from wrap end (stage $\mathbf{i_e}$)	Disp. (mm)	5.39	4.74 [12.1]	-	-
	Load (kN)	341.5	340.7 [0.2]	-	-
Rupture (stage **r**)	Disp. (mm)	6.75	6.60 [2.2]	20.36	19.44 [4.5]
	Load (kN)	346.0	346.5 [0.03]	1640	1659 [1.2]

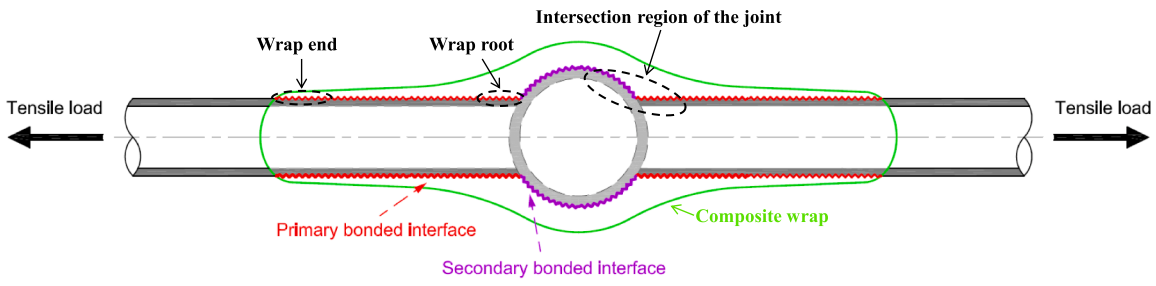

Fig. 14. A schematic overview of identified failure regions during the debonding process of wrapped composite X-joints (cross-sectional view).

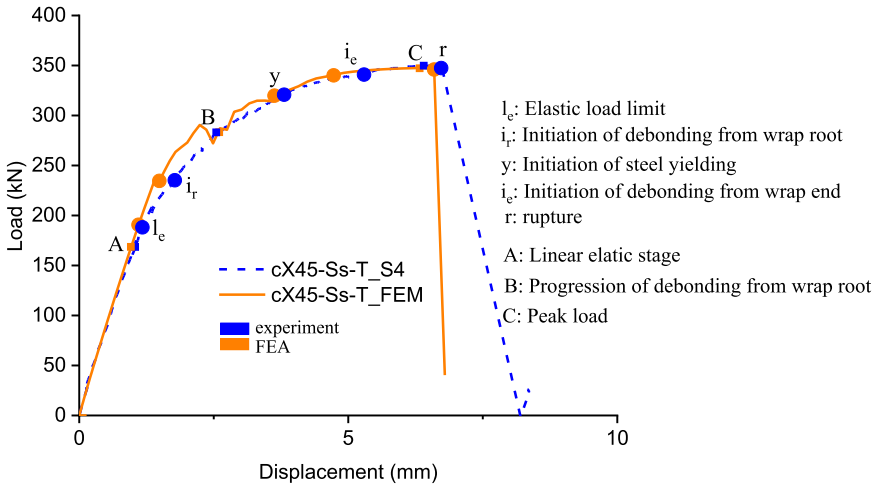

Fig. 15. Load-displacement response for the small-scale joint test specimen X45-Ss-T_S4 and the FE model.

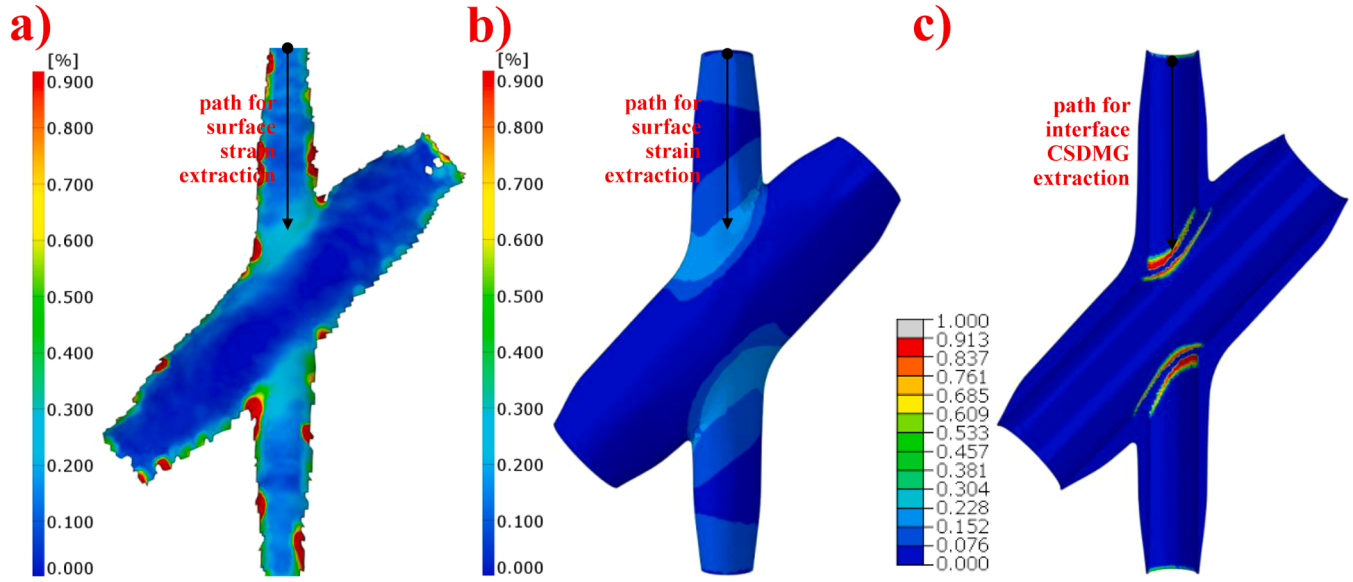

Fig. 16. Surface strains at linear elastic stage (stage A – 170 kN) on a) test specimen and on b) FE model, and c) damage variable of bonded interface of FE model indicating fracture process.

5.2. *Comparison of debonding process of composite-steel interface*

The motivation for the comparison of the interface debonding process in joint experiments and FE models is threefold:

1) Further validate the robustness of the defined modeling strategies and the input parameters in joint FE models;
2) Understand the debonding process and interaction of failure modes of wrapped composite joints by FE models, which cannot be achieved explicitly from experiments;
3) Quantify the threshold of the principal strain on the surface of the composite wrap to identify the debonding crack front in DIC analysis.

To facilitate more effective comparisons of the debonding process, five critical stages are defined: stage $\mathbf{l_e}$ – elastic load limit; stage $\mathbf{i_r}$ – initiation of debonding from wrap root; stage **y** – initiation of steel yielding; stage $\mathbf{i_e}$ – initiation of debonding from wrap end; stage **r** – rupture. A schematic overview of the failure regions during the debonding process is illustrated in Fig. 14. To mitigate the impact of variability in the debonding behavior of X-joints in experiments, comparisons of the failure process is conducted between the FE models and an individual specimen at the small-scale (X45-Ss-T_S4) and the medium-scale (X45-Ms-T_S3), respectively. The values of the applied displacement and the monotonic load at the defined critical stages in the FE models are compared to those of the two specimens, as summarized in Table 5.

5.2.1. *Debonding process in the small-scale joint specimen X45-Ss-T_S4 and the FE model*

Comparisons of the load-displacement behavior between the small-scale specimen X45-Ss-T_S4 and the FE model are shown in Fig. 15 with the critical stages marked by solid circles. The comparison of the load and displacement magnitudes at the critical stages manifests a resilient correlation, with deviations remaining below 6 % in Table 5, except at stage $\mathbf{i_r}$ and stage $\mathbf{i_e}$. A possible reason is underestimation of debonding on the secondary bonded interface and underestimation of debonding at the wrap root in the FE model.

Surface strains (principle strains) of the test specimen X45-Ss-T_S4 and the FE model at the marked stages in Fig. 15 during the interface debonding process are compared in Fig. 16 to Fig. 22. The damage

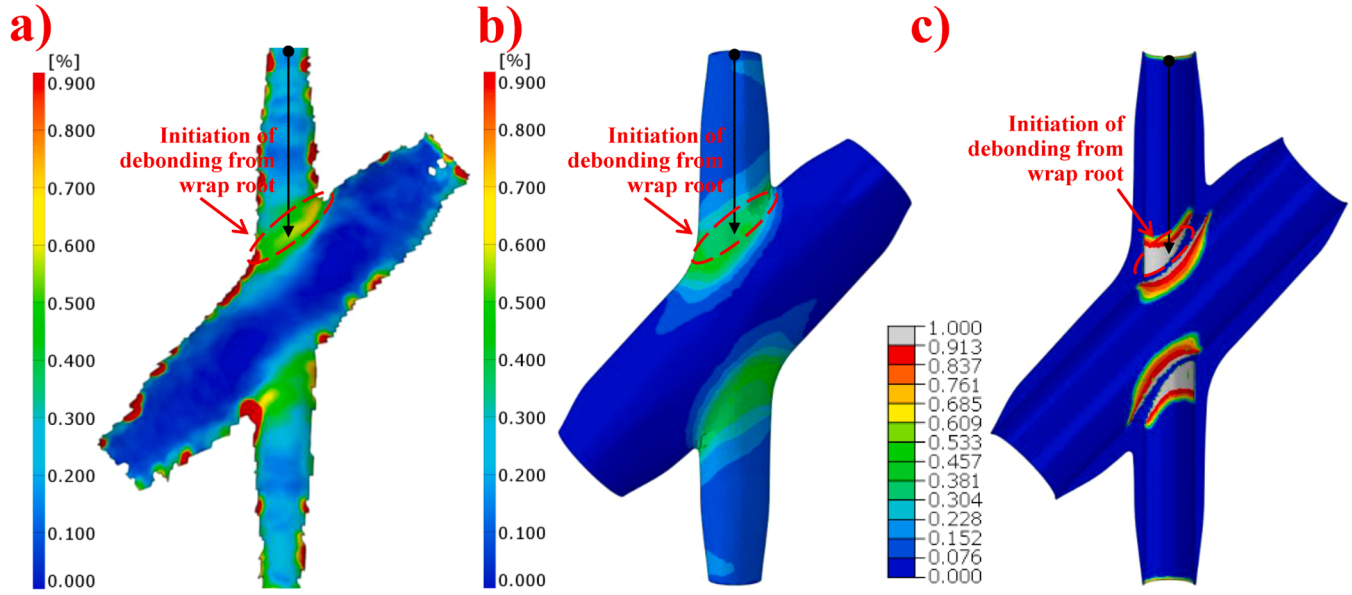

Fig. 17. Surface strains at initiation of debonding from wrap root (stage i_r – 234 kN) on a) test specimen and on b) FE model, and c) damage variable of bonded interface of FE model indicating fracture process.

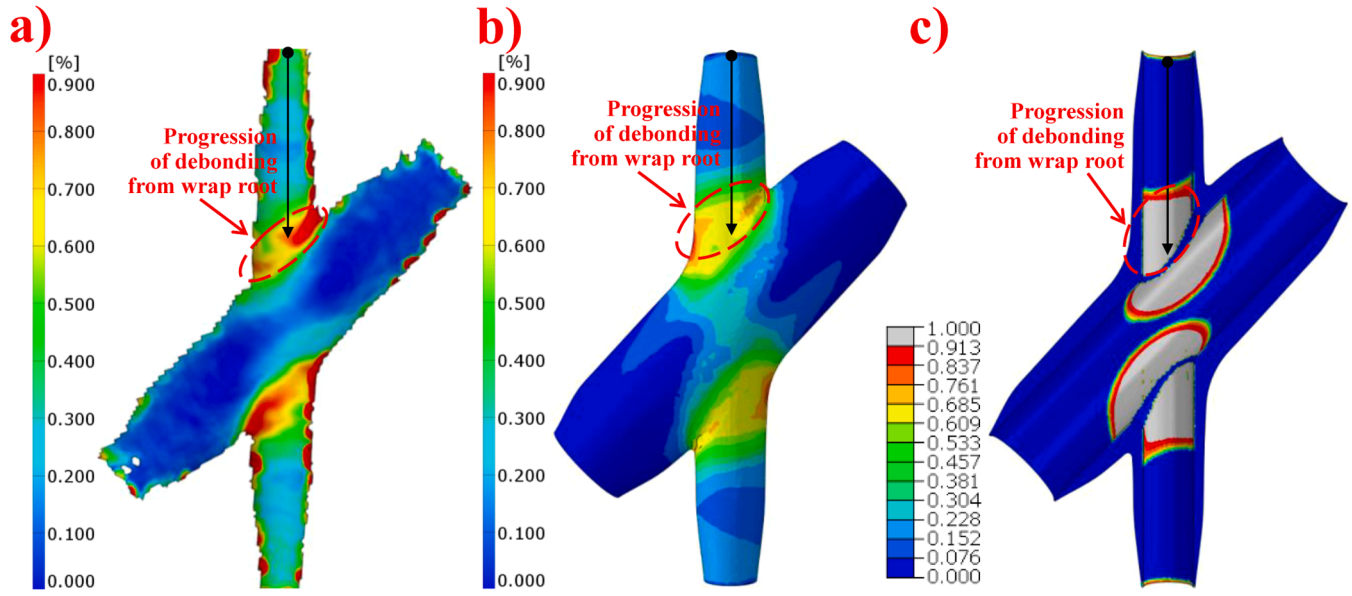

Fig. 18. Surface strains at stage B – 289 kN on a) test specimen and on b) FE model, and c) damage variable of bonded interface of FE model indicating fracture process.

variable output – CSDMG from FEA is also illustrated to visualize the debonding length on the bonded interface.

The joint behaves elastically with low strains distributed uniformly on the joint surface as shown in Fig. 16 – stage **A** at 170 kN. The end of elastic behavior is reached at approximately 180 kN (stage $\mathbf{l_e}$) attributed to plasticity of the bonded interface at the wrap root and local bending of the composite wrap at the middle of the chord member. Debonding on the primary bonded interface is initiated from wrap root due to shear stress concentrations indicated by the localized increase of surface strains and the occurrence of damaged region at the wrap root shown in Fig. 17 – stage $\mathbf{i_r}$ at 234 kN. Debonding on the secondary bonded interface is initiated simultaneously at this stage. Subsequently, the debonding crack propagates steadily along the primary and the secondary bonded interfaces at stage **B** – 289 kN indicated by large regions of elevated surface strain and by large regions of damage at the bonded interface (Fig. 18). The debonding crack is observed to propagate consistently, depicted by continued growth of elevated surface strain regions and the regions of bonded interface damage in Fig. 19 at stage **y** – 321 kN. Meanwhile, yielding of the steel braces is seen to initiate outside the composite wrap. At this stage the regions of debonding on the primary bonded interface is found to be moderately larger in numerical results than in experimental tests results. One potential explanation is linked to the more substantial yield strain found on the braces in the experiments, dissipating a larger proportion of external energy from the loading system and thereby decreasing the strain energy release due to the progression of the debonding crack.

The surface strain of the steel brace becomes excessive at stage $\mathbf{i_e}$ – 341 kN, leading to the contraction of the cross section. This results in development of peel stresses at the interface, leading to a mixed-mode dominated debonding at the wrap end, as shown in Fig. 20. However,

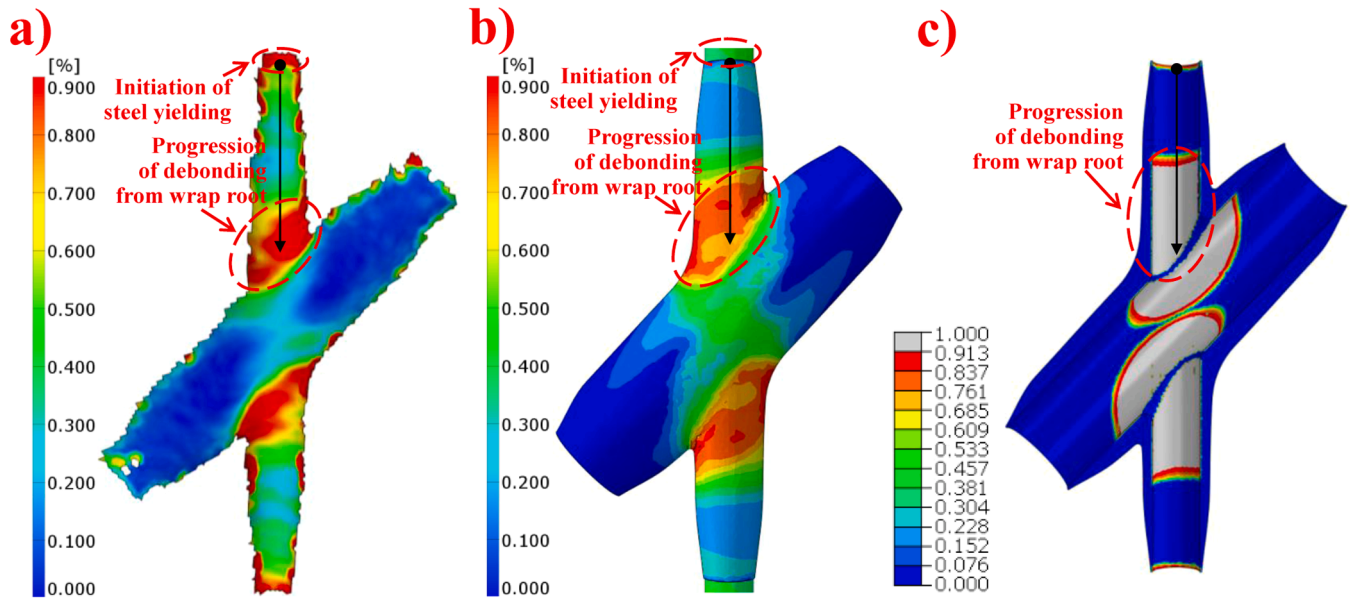

Fig. 19. Surface strains at stage y – 321 kN on a) test specimen and on b) FE model, and c) damage variable of bonded interface of FE model indicating fracture process.

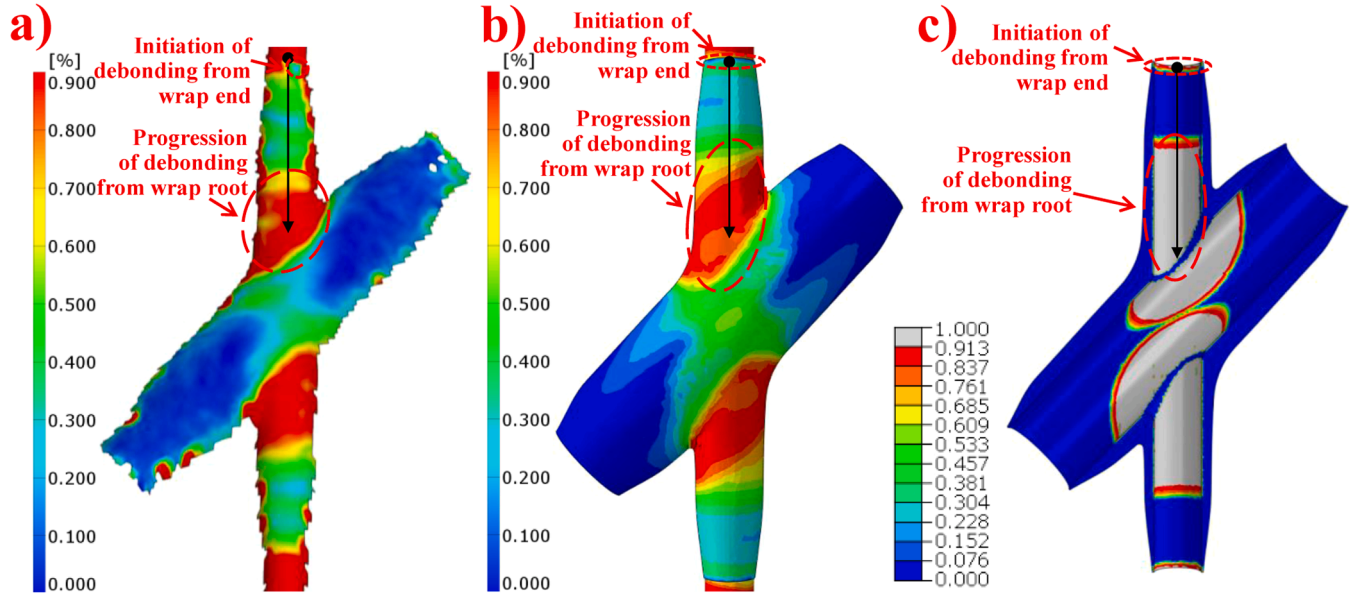

Fig. 20. Surface strains at stage i_e – 341 kN on a) test specimen and on b) FE model, and c) damage variable of bonded interface of FE model indicating fracture process.

as the applied monotonic tensile load increases to its peak magnitude at stage **C**, the mixed-mode debonding process from the wrap end does not propagate further in the FE model (Fig. 21). This is probably due to the overestimation of the interface fracture toughness defined in the mixed-mode cohesive law. Meanwhile, the debonding crack from the wrap root propagates steadily and reaches a maximum length at the rupture stage **r** (Fig. 22) prior to full debonding failure. On the contrary, in the test specimen, the debonding crack propagates significantly from wrap end indicated by a growth of low surface strain regions shown in Fig. 21a. It dissipates most of the strain energy such that debonding from the wrap root ceases to propagate. Subsequently, the debonding crack from the wrap end increases to a critical length at stage **r** (Fig. 22) prior to the final failure due to coalescence of debonding cracks originating from the wrap end and the wrap root.

To quantify the aforementioned debonding progress on the primary bonded interface, a path is defined along the middle of the measured surface in both the test specimen and the FE model, spanning from the wrap end to the wrap root, along which surface strain is extracted. Similarly, a path is defined along the middle of the primary bonded interface in the FE model where the scalar damage variable (CSDMG) is extracted. The surface strains are scaled to the strain level obtained at the elastic stage (stage **A**) to eliminate the strain accumulation due to elasticity and thereby to obtain the strain magnitude exclusively associated with the debonding process. The threshold magnitude of CSDMG (0.913) at stage "c" in the mode II cohesive law (Fig. 11) is utilized to define the debonding crack front location in the FE model. The scaled surface strain magnitude at the crack front is utilized as the threshold strain magnitude to define the debonding crack on the primary bonded

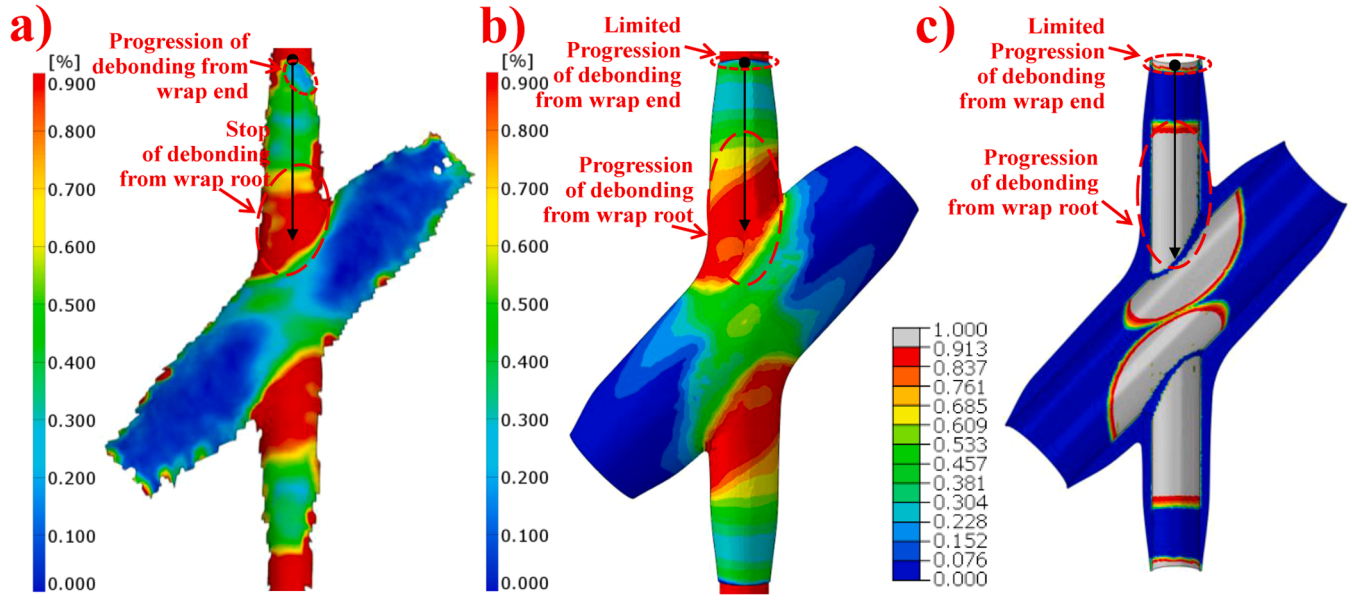

Fig. 21. Surface strains of composite wrap at stage C – 349 / 347 kN on a) test specimen and on b) FE model, and c) damage variable of bonded interface of FE model indicating fracture process.

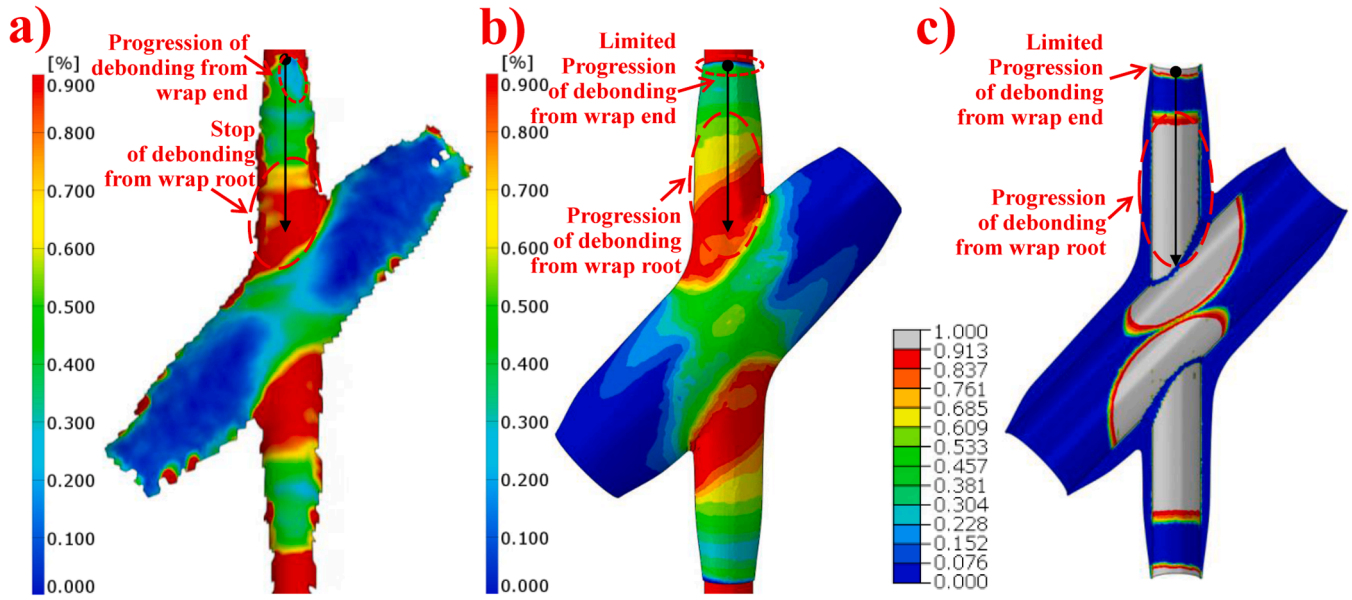

Fig. 22. Surface strains of composite wrap at stage r – 346 kN on a) test specimen and on b) FE model, and c) damage variable of bonded interface of FE model indicating fracture process.

interface in the FE model.

The scaled strain obtained in DIC and in the FE model, as well as CSDMG obtained in the FE model are plotted together in Fig. 23 in solid lines, short dashed lines and dashed lines, respectively, to quantify the debonding length at the critical stages. The debonding crack front at the vicinity of the wrap root and wrap end are identified as the location where the scaled surface strains abruptly increase. However, in the region with unform wrap thickness, the crack front is defined by the threshold surface strain magnitude of 0.06 %. The decrease of surface strain from the wrap root region to the uniform region is steadier in the FE model than in DIC, potentially attributed to differences in ply drops between the model and the test specimens. Moreover, the debonding length is almost identical between DIC and the FE model until stage **y.** Thereon, the more moderate yielding strain on braces obtained in the FE model results to a higher extent of debonding from the wrap root, leading to a larger debonding length. Debonding on the wrap root in experiments ceases to propagate once the load reaches stage $\mathbf{i_e}$ where debonding on the wrap end initiates and significantly propagates until coalescence of both cracks. In contrast, in the FE model the debonding crack on the wrap root consistently propagates to the wrap end, whereas there is limited initiation of a debonding crack observed originating from the wrap end.

In summary, the FE model is able to adequately replicate the debonding process observed in the joint experiments. This substantiates the modeling strategy and the appropriate calibration of the associated input material models.

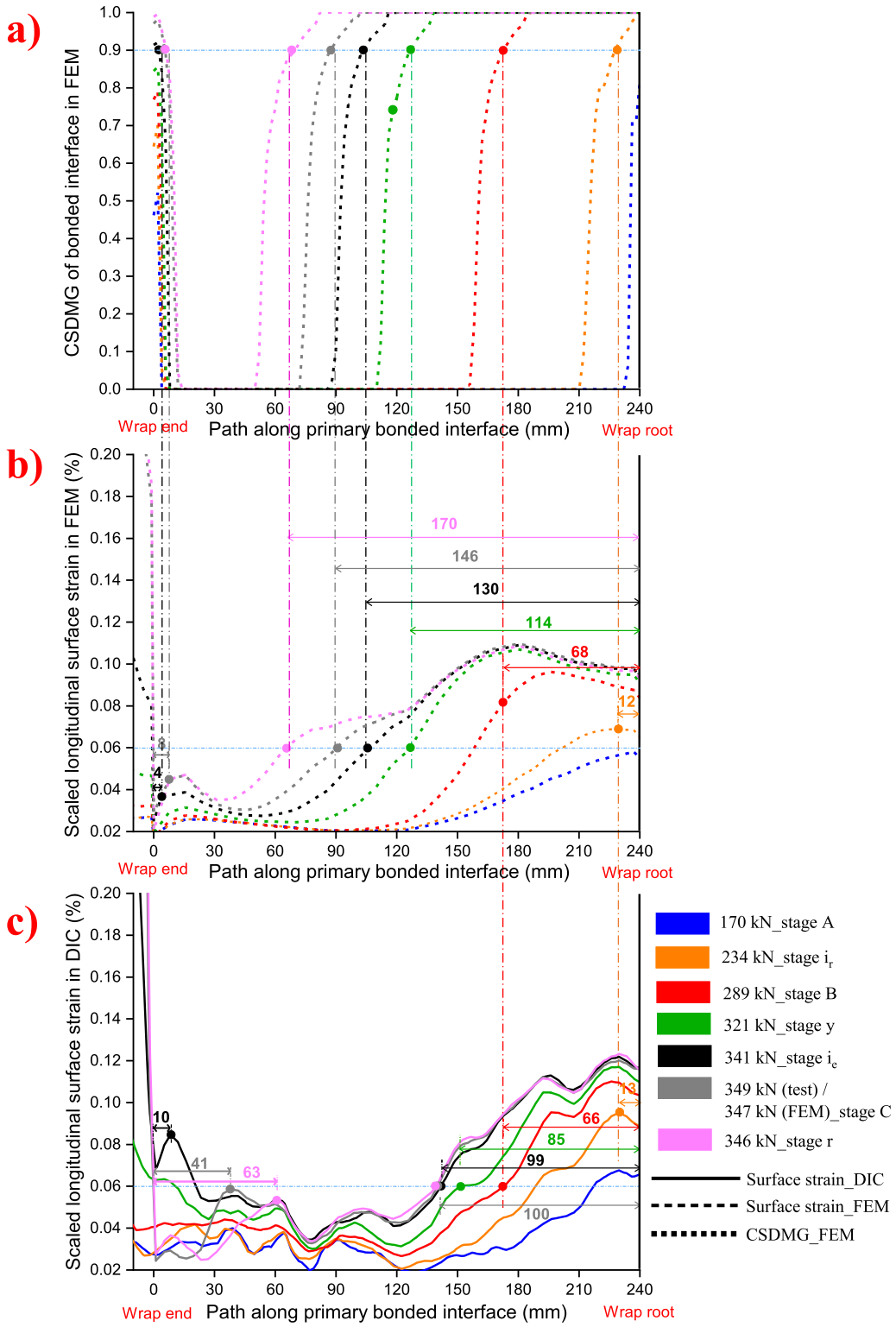

Fig. 23. Scaled surface strains obtained in c) experimental tests (DIC) and in b) FE model (FEM) and a) damage variable along the primary bonded interface at critical loading stages of small-scale 45° X-joints, quantifying the debonding length.

5.2.2. Debonding process in the medium-scale joint specimen X45-Ms-T_S3 and the FE model

Similar to the small-scale joint, a sound alignment in the global response is obtained between the medium-scale specimen X45-Ms-T_S3 and the FE model, as illustrated in Fig. 24. The deviation of displacement and load values between them is within 10 % at all the critical stages except for the displacement at stage $\mathbf{i_r}$ (see Table 5). It can be seen from Fig. 24 that the load drop between 3–7 mm is more sudden in the FE model than in the test specimen. The possible reason is that in the test specimen at medium-scale, the loss of stiffness is due to interaction of chord interface debonding and chord composite wrap leading to a more gradual transition of stiffness. By defining through-thickness shear plasticity using solid element, the FE model can only partially capture the delamination behavior. Therefore, with the current modeling

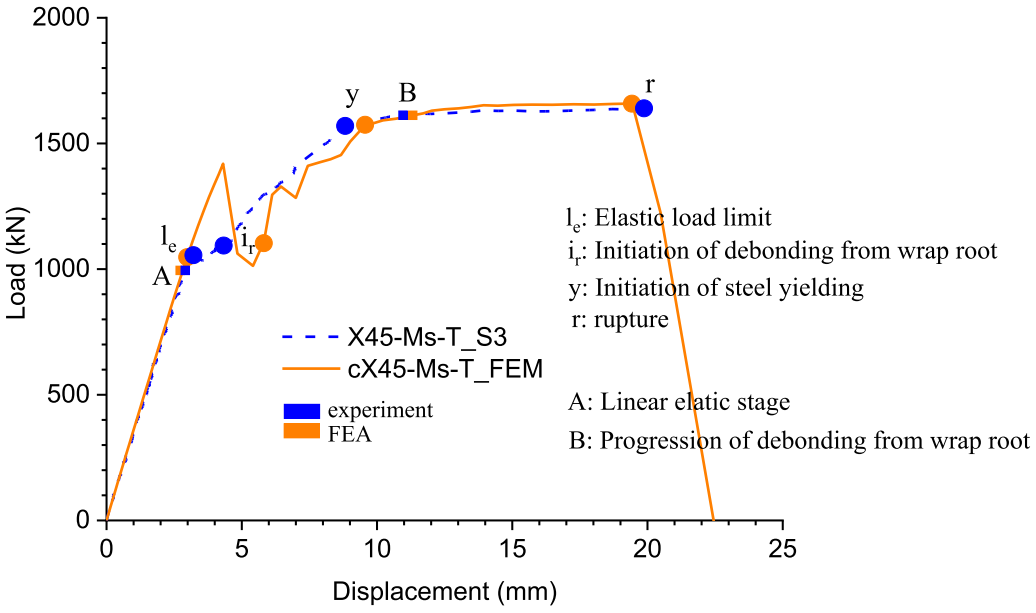

Fig. 24. Load-displacement response of the medium-scale joint test specimen X45-Ms-T_S3 and the FE model.

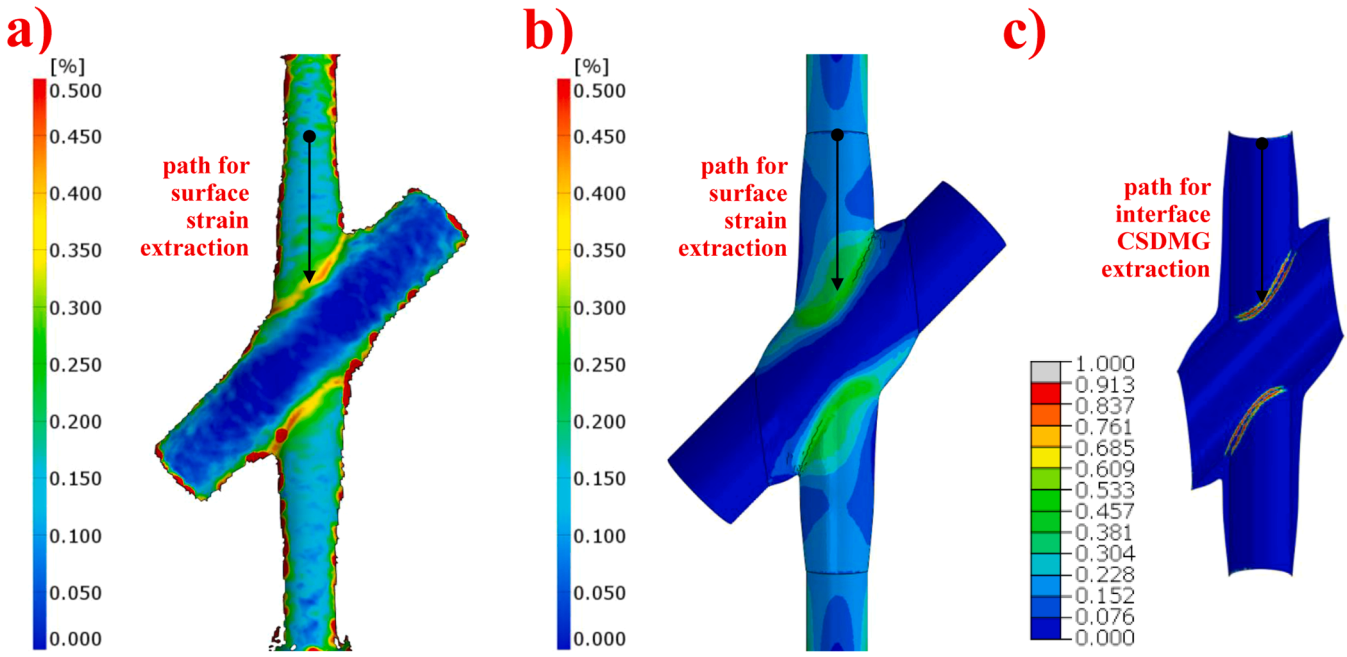

Fig. 25. Surface strains at linear elastic stage (stage A – 1000 kN) on a) test specimens and on b) FE model, and c) damage variable of bonded interface of FE model indicating the fracture process.

strategy, we cannot alleviate the sudden load drop. However, for the design purposes we do not consider it a problem since the ultimate load and the brace debonding process are well aligned between experiments and the simulation.

Surface strains of test specimen X45-Ms-T_S3 and the FE model, as well as the interface CSDMG in the FE model, are compared at the critical debonding stages in Fig.s 25–29. At stage **A** the joint is still in the elastic state with relatively low and uniformly distributed surface strains, as shown in Fig. 25. When stage $\mathbf{l_e}$ is reached, the elastic stage ends due to plasticity of the bonded interface at the wrap root and local bending of the composite wrap. Subsequently, debonding is initiated on the secondary bonded interface and propagates consistently. It is followed by the initiation of debonding on the primary bonded interface at stage $\mathbf{i_r}$ due to shear stress concentrations. It is observed from the surface strain distribution in Fig. 26 that debonding on the chord is overestimated by the FE model presumably attributed to the limitation of the material model in its capacity to simulate the out-of-plane tension behavior of the composite wrap. Nevertheless, the debonding on the brace obtained from the FE model accurately fits that obtained from the experimental model. It features a steady propagation until stage **y** and stage **B**, as shown in Fig. 27 and Fig. 28, respectively. Yielding of the brace is initiated outside the composite wrap at stage **y** however as opposed to small-scale joints yielding does not result in debonding from the wrap end. At stage **r,** debonding on the brace from the wrap root reaches the critical length and leads to the subsequent full debonding (Fig. 29).

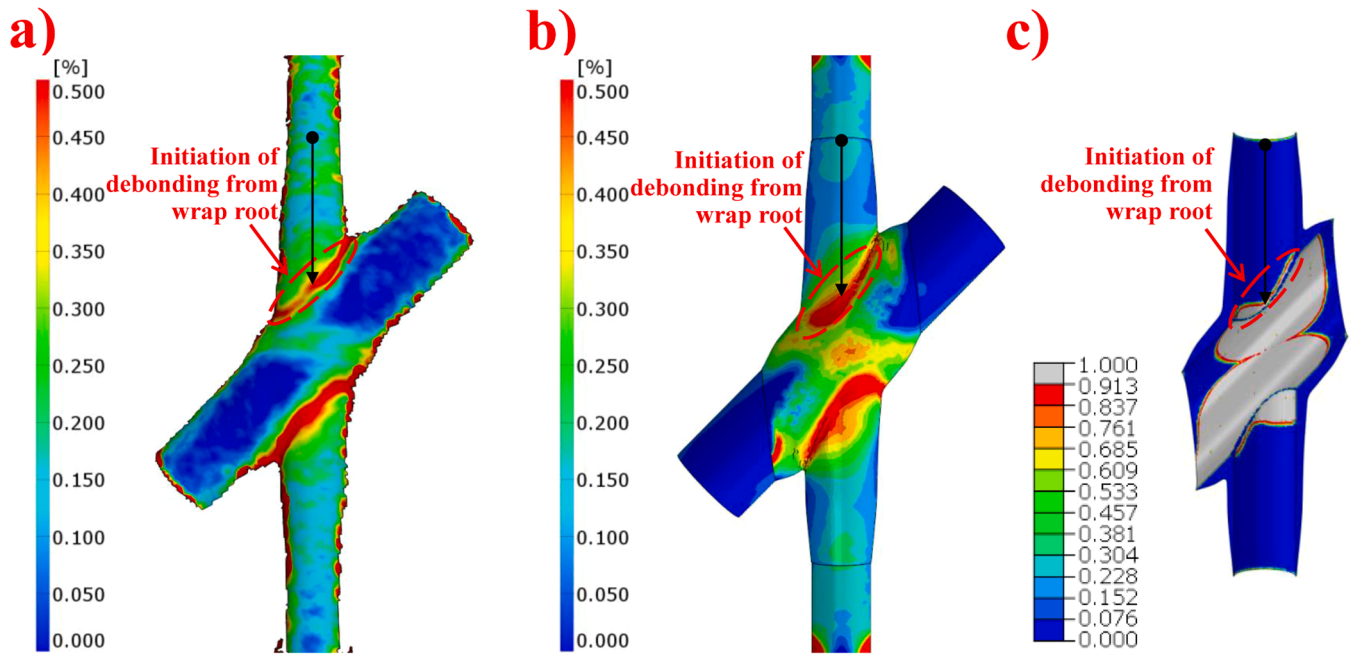

Fig. 26. Surface strains at initiation of debonding from wrap root (stage i_r – 1106 kN) on a) test specimens and on b) FE model, and c) damage variable of bonded interface of FE model indicating the fracture process.

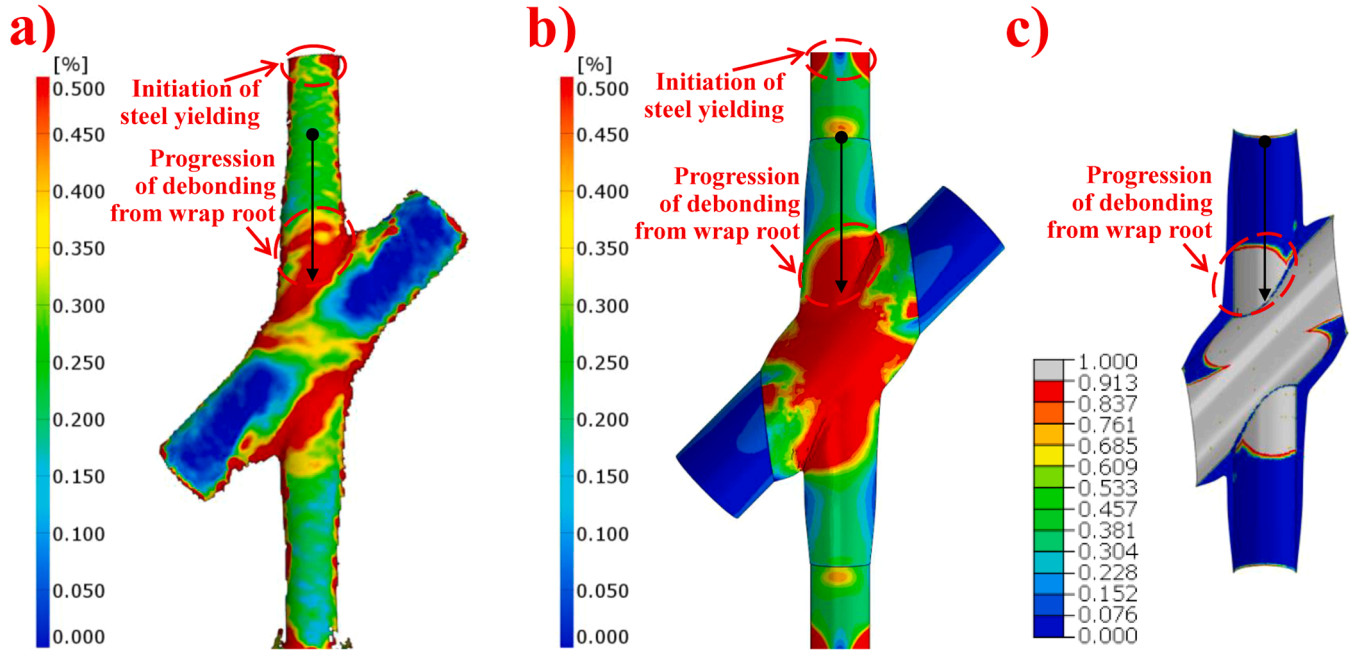

Fig. 27. Surface strains at stage y on a) test specimens (1571 kN) and on b) FE model (1579 kN), and c) damage variable of bonded interface of FE model indicating the fracture process.

Similar to the small-scale joint analysis, a path is defined on the measured surface in both the medium-scale test specimen and the FE model to compare surface strains. Likewise, a path is established on the primary bonded interface in the model to represent the damage variable (CSDMG). The surface strains are scaled to the elastic stage (stage **A**), and the value of CSDMG (0.913) at stage "c" in the mode II cohesive law (see Fig. 11) is utilized to define the debonding crack front location in the FE model.

The scaled path strain obtained in DIC and in the FE model, as well as the CSDMG in the FE model from the respective paths are plotted together in Fig. 30 in solid lines, short dashed lines, and dashed lines, respectively, to quantify the debonding length at the critical stages. The debonding crack front at the vicinity of the wrap root is identified as the location where the strain level abruptly increases. At the uniform wrapping thickness region, the crack front is defined by the threshold surface strain magnitude of 0.1 %. It can be seen that the debonding length is almost identical in DIC and in the FE model for all critical stages. Therefore, the FE model adequately replicates the debonding process observed in the joint experiments. This substantiates the modelling strategy and the appropriate calibration of the associated

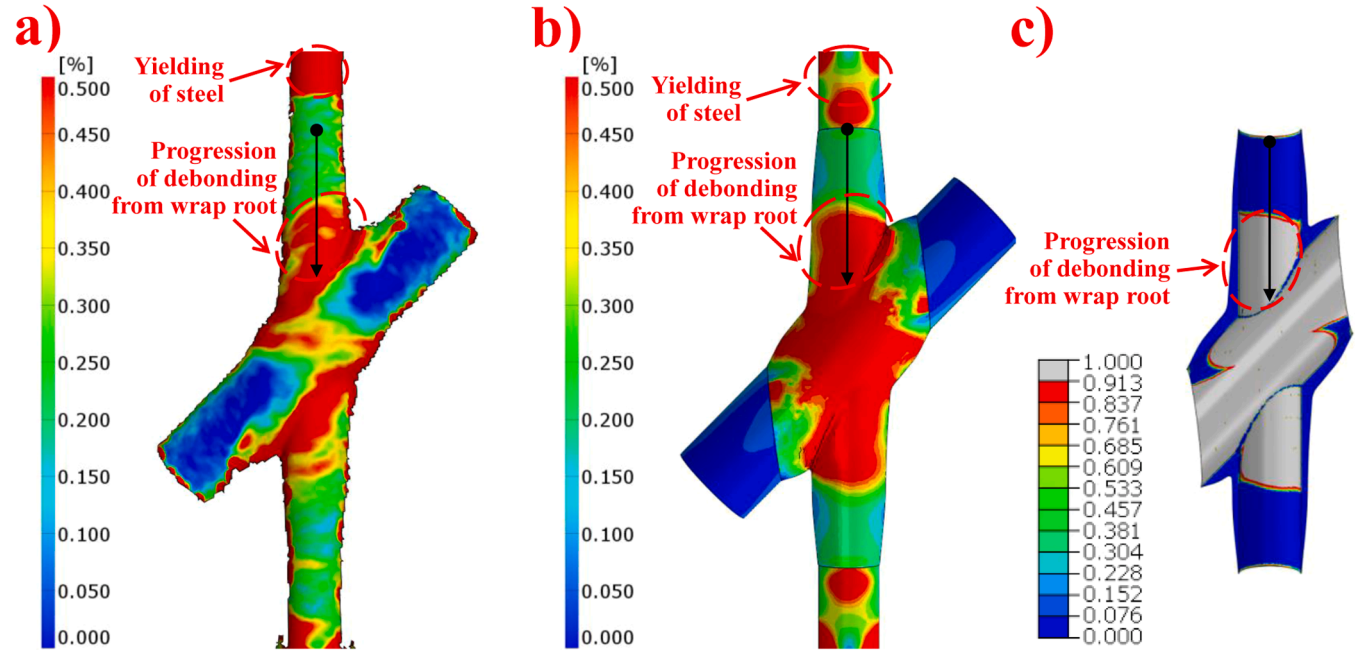

Fig. 28. Surface strains of composite wrap at stage B – 1618 kN on a) test specimens and on b) FE model, and c) damage variable of bonded interface of FE model indicating the fracture process.

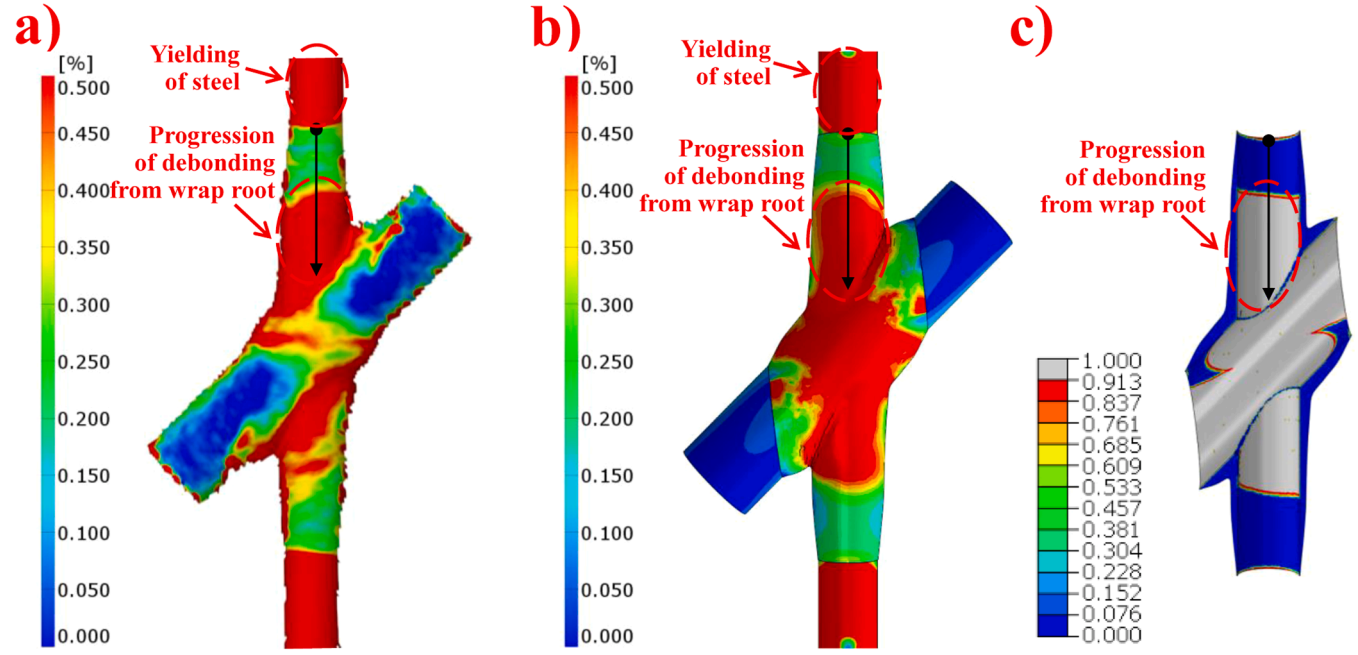

Fig. 29. Surface strains of composite wrap at stage r on a) test specimens (1640 kN) and on b) FE model (1659 kN), and c) damage variable of bonded interface of FE model indicating the fracture process.

input material models.

6. Model updating through sensitivity studies

This section presents the results of modeling updating through sensitivity studies, including a mesh sensitivity analysis and sensitivity studies on COF and mode II interface fracture toughness G_{IIc}.

6.1. Mesh sensitivity study

A mesh sensitivity study was performed on the medium-scale X-joint model using three different element sizes (2 mm, 4 mm used in the numerical validation, and 8 mm) to investigate the influence of element size on joint modeling. Additionally, modeling results using 4-node tetrahedral elements (C3D4) and the 10-node tetrahedral elements (C3D10) were compared at the size of 4 mm to investigate the effect of mesh geometric order.

The comparison is presented using the relative load-displacement

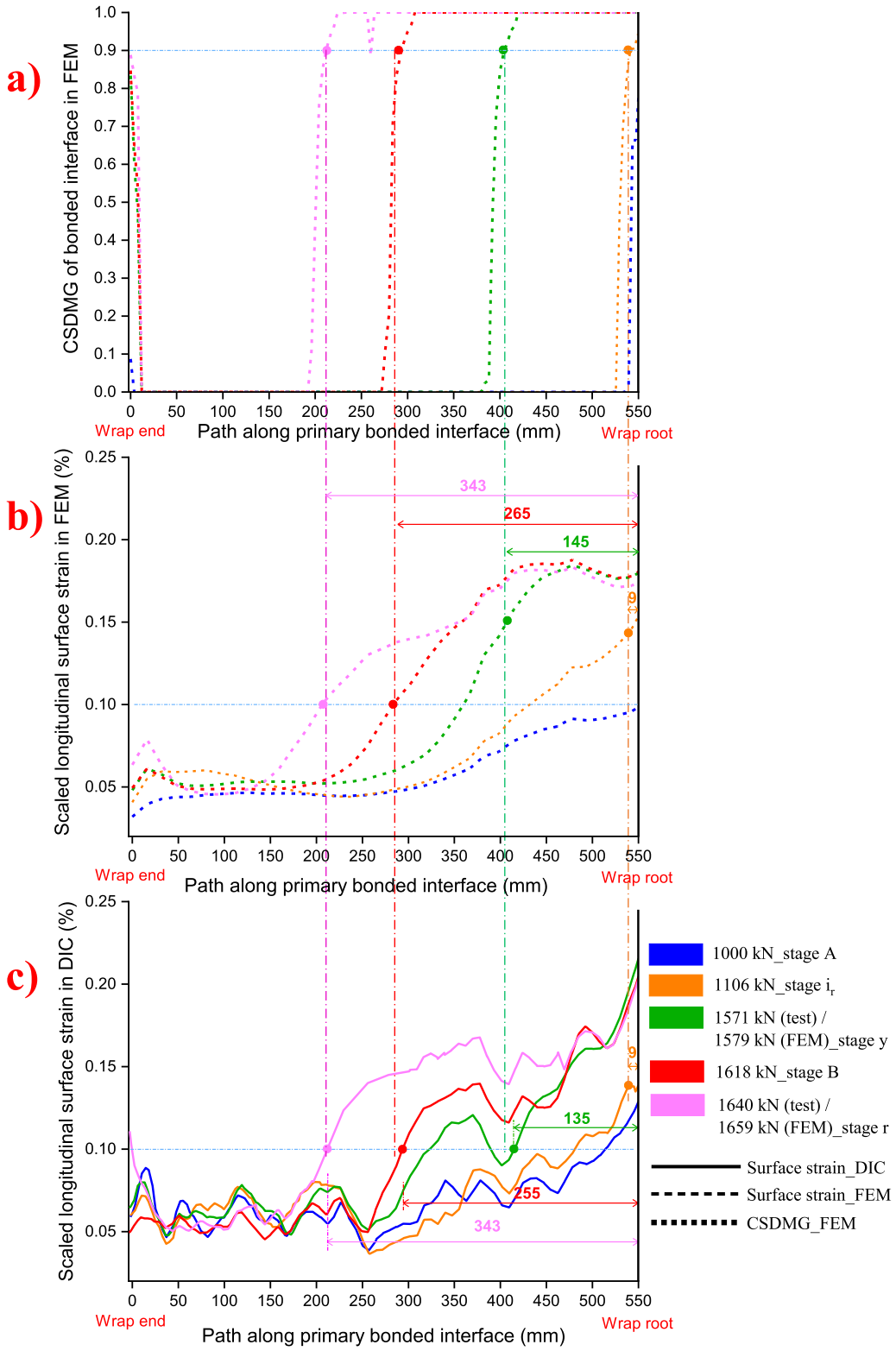

Fig. 30. Scaled surface strains obtained in c) experimental tests (DIC) and in b) FE model (FEM) and a) damage variable along the primary bonded interface at critical loading stages of medium-scale 45° X-joints, quantifying debonding length.

behavior shown in Fig. 31, where the relative failure displacement and the relative ultimate resistance are considered as 100 % using the 4-mm C3D4 element. It can be seen that doubling the reference element size leads to a 4 % increase in ultimate resistance, while halving it results in a 5 % decrease in ultimate resistance. This allows the usage of a medium-size mesh without the risk of overestimating the joint resistance. Moreover, using quadratic elements leads to an 8 % increase in ultimate resistance, exhibiting the same trend as using a smaller element size. Using linear elements saves computational cost and prevents the risk of overestimating the joint resistance. Therefore, in the numerical validation, the material and interface properties used in the joint model were calibrated based on the linear medium-size elements.

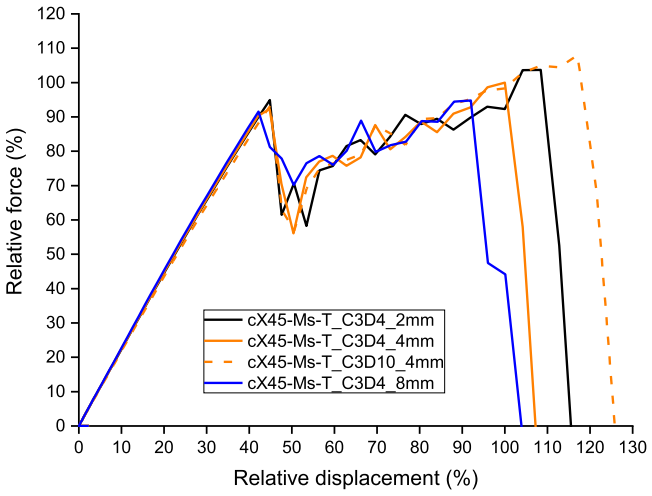

Fig. 31. Relative load-displacement behavior of the medium-scale X-joint model using C3D4 elements with 3 different sizes and using C3D10 elements.

6.2. Sensitivity of coefficient of friction and mode II interface fracture toughness

It can be seen in Section 5 that the load-displacement behavior of small-scale and medium-scale test specimens exhibits variations in ultimate resistance and failure displacement. To explain the variations, the sensitivity analysis was performed on values of COF and mode II interface fracture toughness G_{IIc}.

According to the range of COF values determined by the COF tests performed by the authors [56], three COF values (0.5, 0.55 used in the numerical simulation, 0.6) were used in the sensitivity study. The load-displacement behavior shown in Fig. 32 indicates that at both scales the ultimate resistance and the failure displacement of the joint increase with the COF values with notable sensitivity.

To understand the sensitivity of the joint behavior to the mode II interface fracture toughness, three values of G_{IIc} were used in the medium-scale joint modeling. These values correspond to the reference value used in the numerical validation (1.60 N/mm), and values decreased (1.28 N/mm) and increased (1.92 N/mm) by 20 %, respectively. The load-displacement curves illustrated in Fig. 33 show that the failure displacement and ultimate resistance increase with the value of G_{IIc} with notable sensitivity.

Based on the results of sensitivity studies, it can be concluded that variations in ultimate resistance and failure displacement of the test specimens are due to a combination of variations in the coefficient of friction and mode II interface fracture toughness of their bonded interface.

7. Design recommendations

Based on the results of the numerical modeling in accordance with the joint experiments performed at two scales, a preliminary mechanic-based formula was proposed for the design and application of wrapped composite X-joints, as shown in Eq. 2: [55].

$$\frac{F_r}{\pi d l_{wb}} = A\frac{d}{t_{wn}} + B \tag{2}$$

where F_r refers to the ultimate load, d is the brace diameter, and L_{wb} and t_{wn} refer to the wrapping length on the brace and the nominal wrapping thickness, respectively. A and B are constants. This formula indicates that the average shear resistance of the bonded interface is inversely proportional to the ratio of the brace diameter to the wrapping thickness, see Fig. 34. The values of A and B are −0.67 and 11.64, respectively, according to the linear regression analysis. There might be a non-linear dependency of the average debonding resistance on the d/t_{wn} ratio. However, considering limited test results (only two scales), we assume the dependency is linear and is validated only within the brace

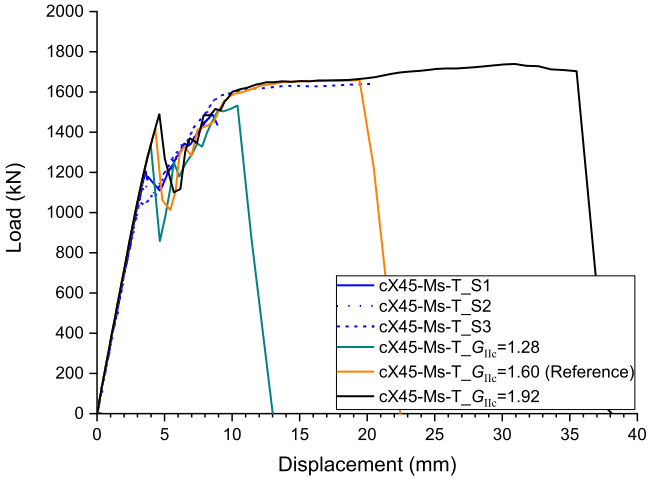

Fig. 33. Load-displacement behaivor of medium-scale joint with different values of G_{IIc}.

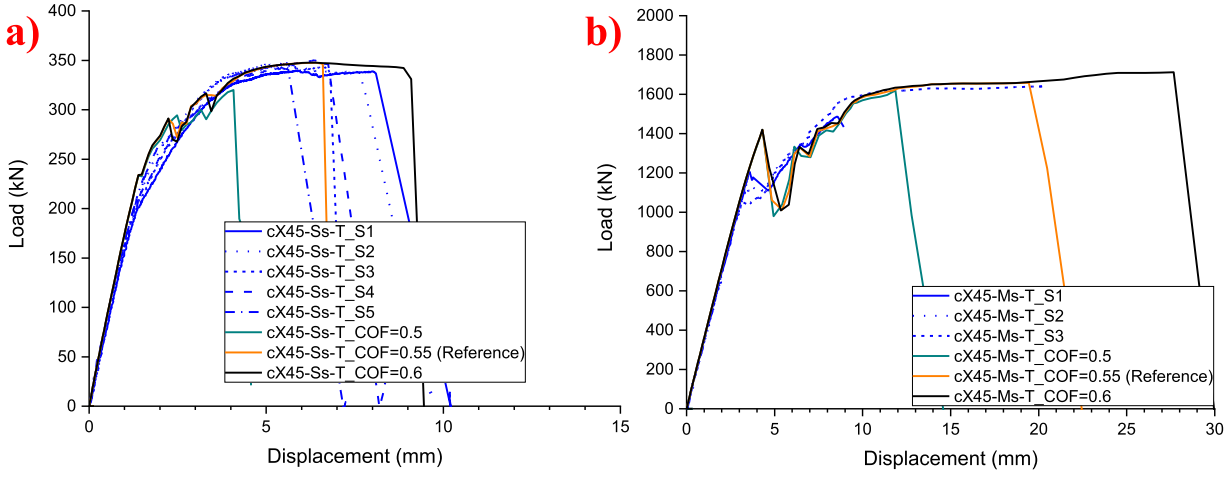

Fig. 32. Load-displacement behavior of small-scale and medium-scale joints with different values of COF.

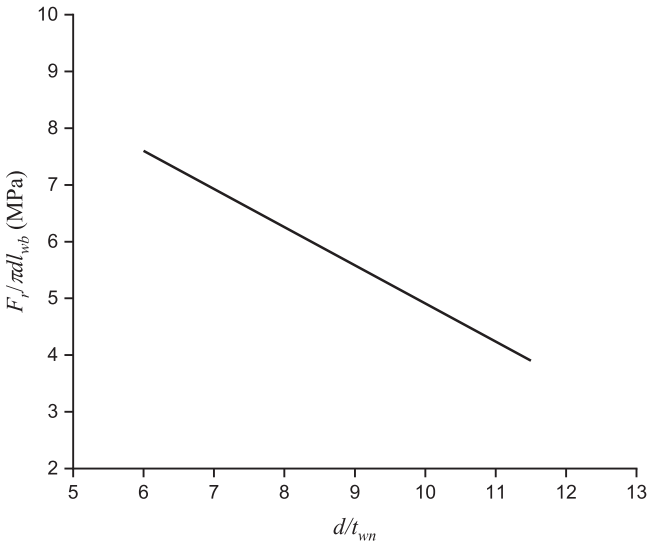

Fig. 34. The relationship between the average shear resistance of the bonded interface and the ratio of brace diameter to wrapping thickness.

diameter range of 60–219 mm and the d/t_{wn} ratio range of 3.9–7.6. Additionally, a wrapping length shorter than 2.5 times the brace diameter is not recommended, based on observations of crack propagation behavior. In the future, for successful application of wrapped composite joints, the interface roughness should be as high as possible, and the high roughness resin should be used.

8. Conclusions

This paper focused on replication of debonding behavior of small-scale and medium-scale wrapped composite 45° X-joints in monotonic tensile tests conducted by the authors [26] using the developed FE models with introduction of new modeling strategies of composite wrap and new interface cohesive law. The FE models were validated by good agreement to the experimental results in terms of global response (load-displacement behavior and ultimate load) and surface path strains analysis throughout the debonding process. Based on the comparisons and the numerical results, the following conclusions can be drawn:

1) When modeling complex composite wrapping geometries that involve significant through-thickness shear deformation but do not exhibit major cracking under monotonic load conditions, it is preferable to model the composite wrap as a 3D solid geometry without defining the layup configuration and to mesh it with 4-node linear tetrahedral (C3D4) elements. The anisotropic plasticity material model is suitable to equivalently and efficiently simulate the overall softening behavior (stiffness degradation) of the laminate due to the aggregate of micro-damage in the matrix, fibers, and the interlaminar interface, etc.
2) Wrapped composite 45° X-joints show rather ductile debonding failure under monotonic tensile load. The elastic resistance of joints is governed by the initiation of debonding. The ductile debonding is attributed to the relatively large fracture toughness on the interface and the remaining friction along the bonded interface which is provided by the circumferential geometry of the joint. The circumferential geometry results in a normal pressure to the bonded interface caused by the circumferential contraction of the composite wrap and Poisson's effect. The ultimate resistance of joints governed by the complete debonding is approximately 40 % larger than the elastic load limit governed by the initiation of debonding.
3) Debonding on the chord leads to loss of joint stiffness while complete debonding on the brace results in ultimate failure. The FE model reveals that in the small-scale joint, debonding starts to propagate simultaneously on the brace and on the chord. Propagation of debonding on the chord is mild and loss of joint stiffness is gradual. In the medium-scale joints, debonding firstly propagates on chord in a more pronounced manner and loss of joint stiffness is abrupt. Once propagation of debonding on the chord is developed to a steady state, debonding starts to propagate on the brace.
4) The preliminary mechanic-based formula was given for calculation of the average shear resistance of the interface within the brace diameter range of 60–219 mm and the d/t_{wn} ratio range of 3.9–7.6. A wrapping length shorter than 2.5 times the brace diameter is not recommended. The interface roughness should be as high as possible, and the high toughness resin should be used for successful application of wrapped composite X-joints.

CRediT authorship contribution statement

Pei He: Writing – original draft, Visualization, Investigation, Formal analysis, Data curation. **Clement Waltener:** Writing – review & editing, Investigation. **Mees Wolters:** Writing – review & editing, Investigation. **Marko Pavlovic:** Writing – review & editing, Supervision, Project administration, Methodology, Funding acquisition, Conceptualization.

Declaration of Competing Interest

The authors declare that they have no known competing financial interests or personal relationships that could have appeared to influence the work reported in this paper.

Data availability

Data will be made available on request.

Acknowledgement

This research is supported by NWO Demonstrator project grant 16949 and RVO project Topsector Energiesubsidie van het Ministerie van Economische Zaken through WrapNode-I project. The first author would also like to express his gratitude for the financial support from China Scholarship Council (CSC) under grant number of 201806260242. The authors are grateful for the acknowledge provision and fabrication of the wrapped composite joints by Tree Composites b.v., Versteden b.v. and Ask Romein b.v. The authors are very grateful for the assistance of technicians from Steven Lab II of TU Delft.

References

[1] Nassiraei H. Static strength of tubular T/Y-joints reinforced with collar plates at fire induced elevated temperature. Mar Struct 2019;vol. 67(December 2018): 102635. https://doi.org/10.1016/j.marstruc.2019.102635.
[2] Nassiraei H. Probability distribution functions for the ultimate strength of X-joints with collar plates in compressive load at room and fire conditions. Structures 2024; vol. 59(December 2023):105703. https://doi.org/10.1016/j.istruc.2023.105703.
[3] Nassiraei H. Probability distribution models for the ultimate strength of tubular T/Y-joints reinforced with collar plates at room and different fire conditions. Ocean Eng 2023;vol. 270(September 2022):113557. https://doi.org/10.1016/j.oceaneng.2022.113557.
[4] Nassiraei H. Local joint flexibility of CHS X-joints reinforced with collar plates in jacket structures subjected to axial load. Appl Ocean Res 2019;vol. 93(March): 101961. https://doi.org/10.1016/j.apor.2019.101961.
[5] Nassiraei H. Geometrical effects on the LJF of tubular T/Y-joints with doubler plate in offshore wind turbines. Ships Offshore Struct 2022;vol. 17(3):481–91. https://doi.org/10.1080/17445302.2020.1835051.
[6] investigation of F. tubular T. under axial compressive loads Lesani MN, Bahaari MR, Shokrieh MM. Numerical investigation of FRP-strengthened tubular T-joints under axial compressive loads. Compos Struct 2013;vol. 100:71–8. https://doi.org/10.1016/j.compstruct.2012.12.020.
[7] Lesani M, Bahaari MR, Shokrieh MM. Experimental investigation of FRP-strengthened tubular T-joints under axial compressive loads. Constr Build Mater 2014;vol. 53:243–52. https://doi.org/10.1016/j.conbuildmat.2013.11.097.

[8] Lesani M, Bahaari MR, Shokrieh MM. FRP wrapping for the rehabilitation of Circular Hollow Section (CHS) tubular steel connections. Thin-Walled Struct 2015; vol. 90:216–34. https://doi.org/10.1016/j.tws.2014.12.013.

[9] Hosseini AS, Bahaari MR, Lesani M. SCF distribution in FRP-strengthened tubular T-joints under brace axial loading. Sci Iran 2020;vol. 27(3 A):1113–29. https://doi.org/10.24200/SCI.2018.5471.1293.

[10] Sadat Hosseini A, Bahaari MR, Lesani M. Parametric study of FRP strengthening on stress concentration factors in an offshore tubular T-joint subjected to in-plane and out-of-plane bending moments. Int J Steel Struct 2019;vol. 19(6):1755–66. https://doi.org/10.1007/s13296-019-00244-0.

[11] Sadat Hosseini A, Bahaari MR, Lesani M. Experimental and parametric studies of SCFs in FRP strengthened tubular T-joints under axially loaded brace. Eng Struct 2020;vol. 213(October 2019):110548. https://doi.org/10.1016/j.engstruct.2020.110548.

[12] Sadat Hosseini A, Bahaari MR, Lesani M. Stress concentration factors in FRP-strengthened offshore steel tubular T-joints under various brace loadings. Structures 2019;vol. 20(April):779–93. https://doi.org/10.1016/j.istruc.2019.07.004.

[13] Nassiraei H, Rezadoost P. Stress concentration factors in tubular T/Y-joints strengthened with FRP subjected to compressive load in offshore structures. Int J Fatigue 2020;vol. 140(May):105719. https://doi.org/10.1016/j.ijfatigue.2020.105719.

[14] Nassiraei H, Rezadoost P. Parametric study and formula for SCFs of FRP-strengthened CHS T / Y-joints under out-of-plane bending load. Ocean Eng 2021; vol. 221(October 2020):108313. https://doi.org/10.1016/j.oceaneng.2020.108313.

[15] Nassiraei H, Rezadoost P. Static capacity of tubular X-joints reinforced with fiber reinforced polymer subjected to compressive load. Eng Struct 2021;vol. 236(May 2020):112041. https://doi.org/10.1016/j.engstruct.2021.112041.

[16] Nassiraei H, Rezadoost P. Stress concentration factors in tubular X-connections retrofitted with FRP under compressive load. Ocean Eng 2021;vol. 229(October 2020):108562. https://doi.org/10.1016/j.oceaneng.2020.108562.

[17] Nassiraei H, Rezadoost P. SCFs in tubular X-connections retro fi tted with FRP under in-plane bending load. Compos Struct 2021;vol. 274(June):114314. https://doi.org/10.1016/j.compstruct.2021.114314.

[18] Nassiraei H, Rezadoost P. SCFs in tubular X-joints retrofitted with FRP under out-of-plane bending moment. Mar Struct 2021;vol. 79(January):103010. https://doi.org/10.1016/j.marstruc.2021.103010.

[19] Rezadoost P, Asgarian B, Nassiraei H. Degree of bending of FRP-reinforced tubular X-joints in offshore jacket-type structures under in-plane bending moment. Ocean Eng 2024;vol. 307(March):118114. https://doi.org/10.1016/j.oceaneng.2024.118114.

[20] Fu Y, Tong L, He L, Zhao XL. Experimental and numerical investigation on behavior of CFRP-strengthened circular hollow section gap K-joints. Thin Walled Struct 2016;vol. 102:80–97. https://doi.org/10.1016/j.tws.2016.01.020.

[21] Xu G, Tong L, Zhao XL, Zhou H, Xu F. Numerical analysis and formulae for SCF reduction coefficients of CFRP-strengthened CHS gap K-joints. Eng Struct 2020;vol. 210(February):110369. https://doi.org/10.1016/j.engstruct.2020.110369.

[22] Sadat Hosseini A, Zavvar E, Ahmadi H. Stress concentration factors in FRP-strengthened steel tubular KT-joints. Appl Ocean Res 2021;vol. 108(September 2020). https://doi.org/10.1016/j.apor.2021.102525.

[23] Zavvar E, Sadat Hosseini A, Lotfollahi-Yaghin MA. Stress concentration factors in steel tubular KT-connections with FRP-Wrapping under bending moments. Structures 2021;vol. 33(June):4743–65. https://doi.org/10.1016/j.istruc.2021.06.100.

[24] M. Pavlovic M. Veljkovic P. Bogers. Method Mak a virgin Jt two Sep Struct hollow Sect, Such a virgin Jt 11 542 2019 708.([Online]. Available:)⟨https://patents.google.com/patent/US11542708B2/en⟩.

[25] "Tree Composites - Technology." [Online]. Available: ⟨https://www.treecomposites.com/over/⟩.

[26] He P, Pavlovic M. Failure modes of bonded wrapped composite joints for steel circular hollow sections in ultimate load experiments. Eng Struct 2022;vol. 254 (August 2021):113799. https://doi.org/10.1016/j.engstruct.2021.113799.

[27] Feng W, Pavlovic M. Fatigue behaviour of non-welded wrapped composite joints for steel hollow sections in axial load experiments. Eng Struct 2021;vol. 249 (October):113369. https://doi.org/10.1016/j.engstruct.2021.113369.

[28] Feng W, He P, Pavlovic M. Combined DIC and FEA method for analysing debonding crack propagation in fatigue experiments on wrapped composite joints. Compos Struct 2022;vol. 297(March):115977. https://doi.org/10.1016/J.COMPSTRUCT.2022.115977.

[29] D.S.S. Corp., ABAQUS/Explicit User's Manual."

[30] I. ANSYS, ANSYS Fluent User's Guide."

[31] R. Eric, The effect of transverse shear deformation on the bending of elastic plates, *J. Appl. Mech.*, 1945.

[32] R.D M. Influence of rotatory inertia and shear on flexural motions of isotropic, elastic plates. J Appl Mech 1951.

[33] L. A.E.H, The small free vibrations and deformation of a thin elastic shell, in *Philosophical Transactions of the Royal Society of London.(A.)*, vol. 43, no. 258–265, London: Royal Society, 1888, pp. 352–353. doi: 10.1098/rspl.1887.0146.

[34] E.J. Barbero, *Finite element analysis of composite materials using Abaqus*. 2013. [Online]. Available: ⟨https://books.google.com/books?hl=en&lr=&id=sKHT0WwTm2UC&pgis=1⟩.

[35] M.P. Wolters, Novel mesoscale modelling method for complex composite geometries Applied onto wrapped composite joints of circular hollow sections, TU Delft, 2020.

[36] Hashin Z, Rotem A. A fatigue failure criterion for fiber reinforced materials. J Compos Mater 1973;vol. 7(4):448–64. https://doi.org/10.1177/002199837300700404.

[37] Shahverdi M, Vassilopoulos AP, Keller T. Mixed-mode quasi-static failure criteria for adhesively-bonded pultruded GFRP joints. Compos Part A Appl Sci Manuf 2014; vol. 59:45–56. https://doi.org/10.1016/j.compositesa.2013.12.007.

[38] Shahverdi M, Vassilopoulos AP, Keller T. Mixed-Mode I/II fracture behavior of asymmetric adhesively-bonded pultruded composite joints. Eng Fract Mech 2014; vol. 115:43–59. https://doi.org/10.1016/j.engfracmech.2013.11.014.

[39] Shahverdi M, Vassilopoulos AP, Keller T. Mixed-Mode I/II fracture behavior of asymmetric composite joints. Procedia Struct Integr 2016;vol. 2:1886–93. https://doi.org/10.1016/j.prostr.2016.06.237.

[40] Cameselle-Molares A, Vassilopoulos AP, Renart J, Turon A, Keller T. Numerical simulation of two-dimensional in-plane crack propagation in FRP laminates. Compos Struct 2018;vol. 200(April):396–407. https://doi.org/10.1016/j.compstruct.2018.05.136.

[41] Heidari-Rarani M, Shokrieh MM, Camanho PP. Finite element modeling of mode i delamination growth in laminated DCB specimens with R-curve effects. Compos Part B Eng 2013;vol. 45(1):897–903. https://doi.org/10.1016/j.compositesb.2012.09.051.

[42] Shokrieh MM, Heidari-Rarani M, Ayatollahi MR. Delamination R-curve as a material property of unidirectional glass/epoxy composites. Mater Des 2012;vol. 34:211–8. https://doi.org/10.1016/j.matdes.2011.08.006.

[43] Sugiman S, Setyawan PD, Salman S, Ahmad H. Experimental and numerical investigation of the residual strength of steel-composites bonded joints: Effect of media and aging condition. Compos Part B Eng 2019;vol. 173(October 2018): 106977. https://doi.org/10.1016/j.compositesb.2019.106977.

[44] N.D. Fernando, Bond Behavior and Debonding Failures in CFRP-strengthened Steel Members, PhD thesis, The Hong Kong Polytechnic University, 2010.

[45] Wang W, De Freitas ST, Poulis JA, Zarouchas D. A review of experimental and theoretical fracture characterization of bi-material bonded joints. Compos Part B Eng 2021;vol. 206(October 2020):108537. https://doi.org/10.1016/j.compositesb.2020.108537.

[46] He P, Arouche M, Koetsier M, Pavlovic M. Mode I fracture behavior of glass fiber composite-steel bonded interface – experiments and CZM. Compos Struct 2023;vol. 330. https://doi.org/10.1016/j.compstruct.2023.117814.

[47] He P, Koetsier M, Mylonopoulos V, Pavlovic M. Mode II fracture behavior of glass fiber composite-steel bonded interface – experiments and CZM. Eng Struct 2024.

[48] He P, Feng W, Pavlovic M. Influence of steel yielding and resin toughness on debonding of wrapped composite joints. Compos Struct 2023;vol. 312(February): 116862. https://doi.org/10.1016/j.compstruct.2023.116862.

[49] International Standards OrganizationISO 6892–1 International Standard INTERNATIONAL STANDARD ISO 6892–1:2009(E) Metallic materials — Tensile testing — Part 1: Method of test at room temperature 1, *Met. Mater.*, vol. 2009, p. 64, 2009.

[50] International Standards OrganizationISO 527–1:2012 - Plastics - Determination of tensile properties - Part 1: General principles, 2012, [Online]. Available: ⟨www.iso.org⟩.

[51] International Standards OrganizationISO 527–2:1996 – Plastics — Determination of tensile properties – Part 2: Test conditions for moulding and extursion plastics, 2009, [Online]. Available: ⟨http://www.chemshow.cn/UploadFile/datum/1000/huayangyq2008w_20094201452507926 88.pdf⟩.

[52] International Standards OrganizationISO 14126:1999 - Fibre-reinforced plastic composites - Determination of compressive properties in the in-plane direction, 1999.

[53] International Standards OrganizationISO 14129: 1997 Fibre-reinforced plastic composites — Determination of the in-plane shear stress/shear strain response, including the in-plane shear modulus and strength, by the plus or minus 45° tension test method, 1997.

[54] Intenational Standards OrganisationISO 19927: 2018 - Fibre-reinforced plastic composites - Determination of interlaminar strength and modulus by double beam shear test, 2018.

[55] Weikang Feng MP, He Pei. Interfacial fatigue debonding retardation in wrapped composite joints: experimental and numerical study. Compos Struct 2023;vol. 319 (April):117146. https://doi.org/10.1016/j.compstruct.2023.117146.

[56] P. He, Debonding Resistance of CHS Wrapped Composite X-Joints, Delft University of Technology, 2023.

[57] Rashid YR. Ultimate strength analysis of prestressed concrete pressure vessels. Nucl Eng Des 1968;vol. 7(4):334–44. https://doi.org/10.1016/0029-5493(68)90066-6.

[58] Cervera M, Chiumenti M. Smeared crack approach: back to the original track. Int J Numer Anal Methods Geomech 2006;vol. 30(12):1173–99. https://doi.org/10.1002/nag.518.

[59] Joki RK, Grytten F, Hayman B, Sørensen BF. A mixed mode cohesive model for FRP laminates incorporating large scale bridging behaviour. Eng Fract Mech 2020;vol. 239(September 2019):107274. https://doi.org/10.1016/j.engfracmech.2020.107274.

[60] Joki RK, Grytten F, Hayman B, Sørensen BF. Determination of a cohesive law for delamination modelling - Accounting for variation in crack opening and stress state across the test specimen width. Compos Sci Technol 2016;vol. 128:49–57. https://doi.org/10.1016/j.compscitech.2016.01.026.

[61] P. He, M.M. Arouche, M. Koetsier, and M. Pavlovic, Mode I fracture behavior of glass fiber composite-steel bonded interface – experiments and CZM, *Compos. Struct. (Minor Revis.*, 2023.